Journal Pre-proof

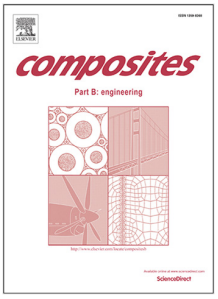

Multiscale Thermodynamics-Informed Neural Networks (MuTINN) for nonlinear structural computations of recycled thermoplastic composites

S.E. Sekkal, M. El Fallaki Idrissi, F. Meraghni, G. Chatzigeorgiou, F. Chinesta

PII: S1359-8368(25)00356-7
DOI: https://doi.org/10.1016/j.compositesb.2025.112455
Reference: JCOMB 112455

To appear in: *Composites Part B*

Received date : 21 February 2025
Revised date : 24 March 2025
Accepted date : 25 March 2025

Please cite this article as: S.E. Sekkal, M. El Fallaki Idrissi, F. Meraghni et al., Multiscale Thermodynamics-Informed Neural Networks (MuTINN) for nonlinear structural computations of recycled thermoplastic composites. *Composites Part B* (2025), doi: https://doi.org/10.1016/j.compositesb.2025.112455.

Multiscale Thermodynamics-Informed Neural Networks (MuTINN) for nonlinear structural computations of recycled thermoplastic composites

S. E. Sekkal[a,b], M. El Fallaki Idrissi[a,c], F. Meraghni[a,*], G. Chatzigeorgiou[a], F. Chinesta[c]

[a] *Arts et Métiers Institute of Technology, CNRS, Université de Lorraine, LEM3-UMR7239, 4 Rue Augustin Fresnel, Metz, 57078, France*
[b] *Cetim, 21 Rue de Chemnitz, Mulhouse, 68200, France*
[c] *ESI Chair, Arts et Métiers Institute of Technology, CNRS, PIMM-UMR 8006, 151 Boulevard de l'Hôpital, Paris, 75013, France*

Abstract

Fiber-reinforced thermoplastic composites are increasingly valued for their lightweight properties, mechanical performance, and recyclability, yet the recycling process introduces microstructural heterogeneities that degrade their mechanical behavior. To address the challenges from a modeling point of view, this study proposes a Multiscale Thermodynamics-Informed Neural Network (MuTINN) approach to predict the nonlinear, anisotropic response of recycled glass fiber-reinforced polyamide 6 composites, with the primary aim of enabling structural simulations in significantly reduced time compared to traditional FE^2 approaches. The MuTINN framework integrates thermodynamic principles with artificial neural networks (ANNs) to capture the evolution of internal state variables and Helmholtz free energy, eliminating the need for memory-based networks. Finite element simulations of representative volume elements (RVEs) under diverse loading conditions are utilized to provide off-line data for the MuTINN. The latter accurately predicts stress, strain, and energy quantities, accounting for the anisotropic and heterogeneous nature of recycled materials. While trained using numerical simulations at 0° and 90° orientation specimens, the proposed framework succesfully predicts the response for specimens with 45° orientation with error in the maximum stress level up to 1.6%. The model is implemented into commercial finite element analysis (FEA) software via a Meta-UMAT

*Corresponding author. Arts et Métiers Institute of Technology, CNRS, Université de Lorraine, LEM3-UMR 7239, 4 rue Augustin Fresnel, 57078 Metz, France

framework, allowing efficient macroscale simulations. Validation against experimental data and finite element-based periodic homogenization confirms the framework's accuracy for structural computations.

Keywords: Mechanically recycled composites, Multiscale nonlinear modeling, Microstructure generation, Artificial Neural Networks, Data-driven modeling

1. Introduction

In recent years, the growing demand for sustainable materials has driven the development and recycling of continuous fiber reinforced thermoplastic composites [1, 2, 3, 4]. These materials, known for their favorable properties such as light weight and high mechanical performance, are increasingly seen as critical to reducing environmental impact across a wide range of industries, including automotive, aerospace, and construction. Indeed, thermoplastic matrices, owing to their meltability compared to non-meltable thermoset polymers, facilitate easier handling in recycling processes, making them particularly suitable for mechanical recycling by shredding or cutting, followed by thermocompression or injection molding processes [1, 4, 5, 6, 7, 8].

Mechanical recycling of thermoplastic composites poses significant challenges due to microstructural changes like porosities, fiber misalignments, and voids, which degrade mechanical properties and limit reuse. Prior research by the authors [9, 10] on recycled polyamide 6 glass fiber composites showed that the recycling process severely disrupts the original woven structure, creating random strand-like composites with increased porosity and resin-rich zones. These alterations resulted in lower mechanical performance and greater variability in material behavior compared to virgin composites. Similarly, Tapper et al. [11] found that in discontinuous carbon fiber polyamide 6 composites, fiber misalignment and breakage during high-compaction recycling led to significant reductions in tensile stiffness and strength after just two cycles. Other recycling techniques using long, chopped unidirectional carbon fiber thermoplastic tapes have reported similar outcomes [4, 12, 13]. However, Kiss et al. [3] offered a promising alternative by co-molding shredded recycled material as a core layer between continuous fiber skins. This sandwich-like structure effectively restored the original laminate's flexural and impact properties, showing potential for upcycling. Controlling processing parameters remains key to optimizing the mechanical performance of these recycled composites. Understanding and predicting their mechanical response is critical to advancing their use in a circular economy, with numerical simulations playing a vital role in refining these approaches.

The modeling of the mechanical response of recycled composite materials, and its link to processing and microstructural parameters, remains relatively underex-

plored. A deep understanding of the complex microstructures induced by recycling is essential for accurate property predictions. While research on prepreg platelet molded composites (PPMCs) and randomly oriented strand composites offers valuable insights, these have not been fully applied to recycled thermoplastic composites. Harper et al. [14] introduced a geometric modeling approach to simulate random fiber architectures in discontinuous fiber composites, facilitating effective mechanical property predictions. Nachtane et al. [9] adapted this model for flexural test simulations on recycled glass fiber composites using a meso-macro framework. Additionally, Tang et al. [15] contributed to this field by investigating the fatigue behavior of chopped carbon fiber composites, utilizing both experimental data and numerical methods to understand their performance under cyclic loading. Kravchenko et al. [16, 17, 18] provided further insights by conducting computational analyses on PPMCs, with a focus on the stochastic meso-scale morphology and its influence on tensile properties under uniaxial tension. Their study employed progressive failure analysis to simulate tensile property distributions, demonstrating how platelet geometry contributes to variations in mechanical performance. Building on these prior works, the authors developed a multiscale model for glass fiber composites that accounts for the microstructural complexity and degradation caused by the recycling process [10].

Traditional modeling methods have played an important role in understanding the mechanical behavior of recycled composites. However, as microstructures become more complex and faster design processes are needed, AI-driven approaches are being explored to speed up and improve material predictions. The rapid growth of Artificial Intelligence (AI), made possible by large datasets, evolving algorithms, and stronger computational power [19, 20], has gained a lot of attention. AI is now widely recognized for its ability to solve complex engineering challenges across various fields [21, 22]. This shift has introduced a new phase in materials science, where data-driven methods like Machine Learning (ML) work alongside traditional experimental, theoretical, and simulation-based approaches [23, 24]. For composite materials, AI techniques such as machine learning and deep learning [25, 26, 27, 28, 29, 30] are increasingly used together with Model Order Reduction (MOR) methods, Self-Clustering Analysis (SCA) [31], and Proper Generalized Decomposition (PGD) [32, 33, 34].

Modeling materials with time-dependent behaviors presents significant challenges. To address these challenges, considerable efforts are focused on developing specialized machine learning and deep learning tools designed for the complex nature and inelastic behaviors of these materials [35, 36]. One approach is Deep Material Networks (DMN), which uses interconnected basic elements for multiscale material modeling [36, 37, 38]. While DMNs can describe various microstructural responses in elastic

and plastic behaviors, they have difficulty with complex microstructures. Alternative methods using Recurrent Neural Networks (RNNs) have also been developed, incorporating components like Long Short-Term Memory (LSTM) and Gated Recurrent Units (GRU) [26, 27, 39, 40, 41]. These models convert input sequences into output sequences for strain and stress tensors. Although RNNs can effectively predict history-dependent behaviors without needing Internal State Variables (ISVs), they face several issues, such as requiring a lot of training data and difficulties in generalizing beyond the training dataset. A recent paper has addressed these limitations in modeling short fiber-reinforced composites by combining recurrent neural networks (RNNs) and transfer learning techniques [25]. By leveraging GRU-based RNNs trained with mean-field simulations and refined using high-fidelity full-field data, the model achieves a balance between computational cost and prediction quality. To improve stability and accuracy, researchers have introduced constraints from physics, leading to Physics-Informed Neural Networks (PINNs), which reduce the need for large training datasets [42, 43, 44]. Building on the PINN concept, Thermodynamics-based Artificial Neural Networks (TANN) have been created [45, 46, 47]. One can cite also the recent relevant work considering fracture mechanics [48]. These models integrate thermodynamic principles into artificial neural networks (ANNs), ensuring consistent predictions for both training (seen) and test (unseen) datasets. TANN models take inputs such as current stress, strain, ISVs, and strain increments, and produce outputs like free energy, dissipation rate, and updated ISVs and stress.

Inspired by PINN and TANN aproaches, the Multiscale Thermodynamics-Informed Neural Networks (MuTINN) model was developed by Idrissi et al. [49]. MuTINN employs two sequential neural networks to establish macroscopic constitutive relationships for inelastic heterogeneous materials, integrating fundamental thermodynamic principles. The first network captures the evolution law, while the second delineates the state law. By defining specific internal state variables (ISVs) at the macroscale, derived from microscale averages, MuTINN eliminates the reliance on memory-based networks, such as RNNs. Additionally, a Meta-UMat framework has been developed to facilitate the integration of MuTINN-based ANN models into commercial finite element software. The effectiveness of this approach has been validated through applications on woven composites exhibiting elastoplastic behavior, showcasing exceptional performance across various loading conditions.

Building on the MuTINN framework, this work introduces key innovations to advance the modeling of recycled thermoplastic composites, focusing on their complex microstructures and mechanical behavior after recycling. The model is trained on datasets produced by periodic homogenization simulations on RVE that has been generated using the Random Sequential Adsorption scheme [50, 10]. The off-line anal-

ysis covers a wide range of loading conditions to ensure its accuracy in practical applications. The homogenization analysis is performed in the nonlinear regime, accounting for the complex microstructure of the thermoplastic-based recycled composites, in which every phase is described in a consistent thermodynamic way. The MuTINN model enables macroscale structural finite element analysis (FEA) for the studied recycled composites, which inherently have a highly heterogeneous microstructure. The advantage is that the new framework allows for accurate macroscale FEA while accounting for microstructural effects, significantly reducing computation time and speeding up material development.

The manuscript is organized as follows: Section 2 discusses the composite recycling process, detailing the microstructural analysis and mechanical response of recycled materials. Section 3 focuses on multiscale modeling of recycled glass fiber reinforced polyamide 6 composites, covering the theoretical background on periodic homogenization and the constitutive laws for strands and matrix. Section 4 defines the quantities of interest and outlines the MuTINN model architecture. Section 5 addresses data generation, presenting results and discussions at the representative volume element (RVE) scale, including model training and validation. Finally, Section 6 showcases the application of MuTINN for structural finite element analysis of recycled composites, highlighting its capacity to incorporate microstructural effects into macroscale computations.

2. Composite recycling process, microstructure analysis, and modeling mechanical response

2.1. Recycling process, microstructural analysis and mechanical response

The recycled composites examined in this study are produced by Cetim, a Research and Technology Organization (RTO) specializing in mechanical recycling of polymer composites. Their "Thermosaïc®" modular production line converts end-of-life components and production waste into consolidated plates via compression molding.

The process begins with shredding the material into small chips, which are evenly distributed for effective consolidation. The chips undergo two compression stages: the first stage pre-heats and pre-compacts the strands at a load below 50 kN and temperature of 240°C, which is below the resin's fusion point. In the second stage, the temperature and load are increased (up to 1300 kN and 300°C) to facilitate proper matrix fusion while preventing unwanted squeeze flow. After forming, the Thermosaïc® plate is cooled and ejected from the production line.

This study focuses on recycled composites made from uniformly sized chips measuring 20 x 20 x 1 mm. The original material is a PA-GF woven composite (Tepex®

Dynalite 102-RG600(x)/PA-GF/47%) supplied by Bond-Laminates GmbH, featuring a fiber volume fraction of 47%. The resulting recycled plate has a thickness of 5 mm and will be referred to as RTPC (Recycled ThermoPlastic Composite).

To understand the properties and behavior of the RTPC, a detailed microstructural investigation was conducted. Figure 1 summarizes this investigation, utilizing both non-destructive and destructive techniques. A macroscale analysis, achieved by burning off the matrix and leaving the reinforcement intact, reveals a significantly heterogeneous structure on the specimen's surface. The dominant feature is a randomly oriented fiber arrangement, with only a few woven fibers remaining intact. This change is attributed to the high pressure and temperature experienced at the mold interface, leading to the degradation of the woven fiber structure.

In addition to the macroscale findings, X-ray tomography shows that the woven structure remains intact at the center of the plate throughout its thickness, as illustrated in Figure 1. However, several strands of fiber bundles exhibit random orientations. Notably, some sections deviate from the original 0° and 90° yarn orientations, likely due to material flow during thermocompression.

Further analysis using optical microscopy reveals that the composite microstructure can be assessed at two distinct scales: microscopic and mesoscopic. This distinction arises from the uneven matrix distribution within the material, as depicted in Figure 1. The heterogeneity is characterized by regions rich in matrix material and others dominated by fibers. At the mesoscopic scale, fibers display a wave-like arrangement with a predominant in-plane orientation, while the microscopic scale presents a more uniform microstructural morphology within the strands, where multiple fibers align similarly.

Collectively, these microstructural insights provide quantitative data for numerical simulations, enhancing the understanding of the material's microstructure, particularly regarding volume fractions at relevant scales. At the microscale, the average fiber ratio within a strand, denoted as $v_{f/s}$, is measured at 75.36%. Meanwhile, at the mesoscale, the strand ratio in the composite, calculated from a global fiber volume fraction of 47% derived from matrix burn-off, is determined to be 62.36%. This information is critical for the microstructure generation process that precedes multiscale modeling.

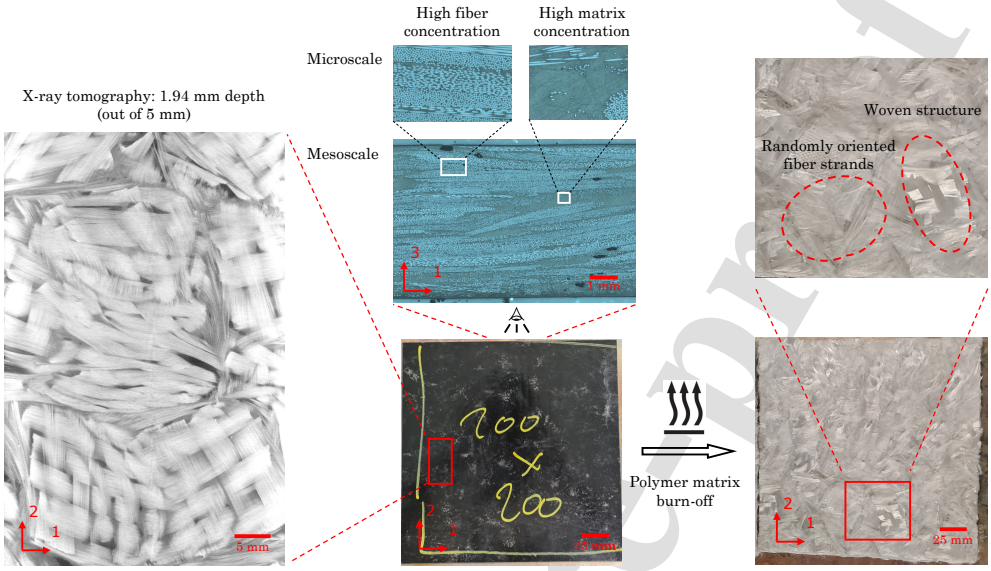

Figure 1: (a) In-plane microstructure of recycled material through X-ray tomography. (b) Optical light microscopy image of the RTPC microstructure, showing observed heterogeneities that lead to an analysis by scale separation. (c) Closeup view of the fiber structure on the surfaces of the specimens after calcination of the polyamide matrix.

Understanding the microstructural characteristics of the RTPC material at all relevant scales, it is essential for predicting their mechanical behavior. Tensile tests conducted on specimens with various orientations revealed a notable difference in mechanical response between the 0° (manufacturing direction) and 90° orientations [10]. This discrepancy can be attributed to the intricate material flow within the mold during thermocompression, which likely resulted in a greater alignment of fibers in the 0° direction, contributing to increased stiffness. Consequently, it can be concluded that the RTPC material does not exhibit macroscopically transversely isotropic properties as initially anticipated, but instead shows some degree of anisotropy.

2.2. Microstructure generation and multiscale modeling of recycled composites

A multi-scale model typically relies on a Representative Volume Element (RVE) that captures the microstructural morphology of the composite, allowing for an objective assessment of its mechanical response. The main challenge in generating a mesoscale RVE for Recycled ThermoPlastic Composite (RTPC) in this research is

achieving the high strand volume fraction needed to accurately represent the material's real microstructures. To address this, the RVE is constructed periodically across multiple layers, rather than placing inclusions directly in a 3D RVE. This approach not only ensures a more accurate representation of the microstructure but also enables the application of periodic boundary conditions for full-field computations. The microstructure generation algorithm follows the Random Sequential Adsorption (RSA) approach [50, 51, 52, 53]. Strands are sequentially placed without intersections in each RVE layer, following a user-defined Orientation Distribution Function (ODF), until the desired strand ratio is achieved.

To maintain the random structure of the RVE while ensuring periodicity by construction, strands intersecting a boundary are duplicated on the opposite side, and those in corners are duplicated across all adjacent corners. Extensive details regarding the microstructure generation process can be found in [10]. Figure 2 shows three examples of generated RVEs with 20 x 20, 30 x 20, and 40 x 20 strands. The strands are arranged in four layers and embedded in a transparent matrix for clarity. For the analysis conducted in this work, an RVE unit cell is comprised of multiple layers. Each RVE, measuring $100 \times 100 \times 5$ mm^3, consists of four layers. Within these layers, strands of 20×20 mm are deposited until saturation (with a volume fraction $v_{s/c}$ of 56%), while ensuring a defined spacing between them to prevent high stress concentration. It is worth noting that the strand, or chip, size is a fixed parameter, since it is determined by the material shredding process.

Tensile tests on Recycled ThermoPlastic Composite (RTPC) showed notable differences in mechanical responses between the 0° and 90° orientations, indicating that the material is anisotropic rather than macroscopically transversely isotropic. This anisotropy arises from fiber alignment during thermocompression, leading to a stiffer 0° direction. To model this, a specific Orientation Distribution Function (ODF) was applied during microstructure generation, but quantifying an ODF experimentally is challenging. Thus, a numerical approach was used to create multiple Representative Volume Elements (RVEs) with varying ODFs to align with experimental observations.

Initially, the strands were simplified as a unidirectional composite based on microstructural analysis. A mean-field Mori-Tanaka homogenization scheme estimated the strand properties but resulted in overestimated mechanical responses. This discrepancy is likely due to fiber damage during processing. To refine the model, a calibration process introduced a correction coefficient accounting for the strands' complexity and degradation. Post-calibration, Young's and shear moduli from micro-homogenization were reduced by 35%, aligning the values for randomly oriented strand RVEs with experimental results. For more on model adjustments to reflect

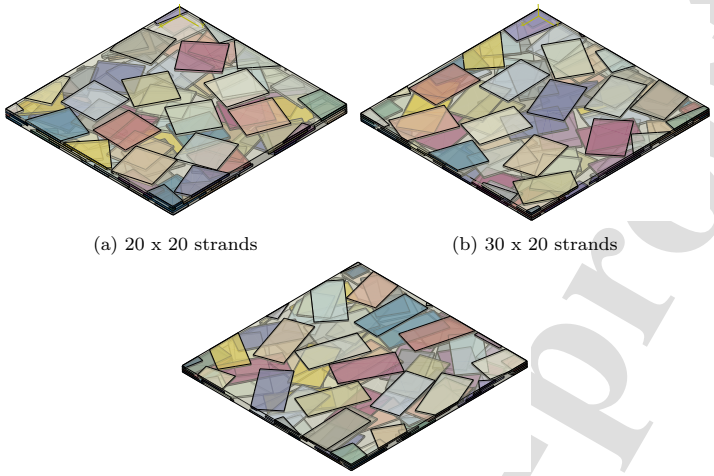

(a) 20 x 20 strands (b) 30 x 20 strands

(c) 40 x 20 strands

Figure 2: Examples of generated Representative Volume Elements (RVEs) for Recycled Thermo-Plastic Composites (RTPC) with strand configurations of (a) 20 x 20, (b) 30 x 20, and (c) 40 x 20. The strands are organized into four distinct layers and are displayed within a transparent matrix to enhance visibility.

microstructural effects, refer to [10].

3. Multiscale modeling of recycled glass fiber reinforced polyamide 6 composites - Experimental validation

3.1. Theoretical background on periodic homogenization

Generating a dataset for training and evaluating MuTINN necessitates employing high-fidelity simulations that yield excellent accuracy and consistency in the predictions of artificial neural networks (ANNs). To achieve this, periodic homogenization-based multiscale methods present an ideal framework, particularly given the hierarchical nature of the microstructure outlined in Section 2.1. This methodology not only facilitates the creation of a robust dataset but also establishes a strong connection between the microscopic and macroscopic scales, ensuring a reliable representation of the material's behavior. This connection requires averaging the stress and strain over the RVE domain $\mathfrak{B}$. Therefore, the macroscopic stress, strain and Helmohltz free energy are given by:

$$\overline{\boldsymbol{\sigma}}(t) = \frac{1}{V} \int_{\mathfrak{B}} \boldsymbol{\sigma}(\boldsymbol{x}, t) \, \mathrm{d}V, \tag{1a}$$

$$\overline{\boldsymbol{\varepsilon}}(t) = \frac{1}{V}\int_{\mathfrak{B}} \boldsymbol{\varepsilon}(\boldsymbol{x},t)\ \mathrm{d}V, \tag{1b}$$

$$\overline{\Psi}(t) = \frac{1}{V}\int_{\mathfrak{B}} \Psi(\boldsymbol{x},t)\ \mathrm{d}V, \tag{1c}$$

where V represents the volume of the Unit Cell (UC) domain $\mathfrak{B}$.

Assuming the Representative Volume Element (RVE) can be represented as a repeating unit, it can be idealized as a periodic unit cell where the displacement field $\boldsymbol{u}$ is expressed additively as follows:

$$\boldsymbol{u}(\boldsymbol{x}) = \overline{\boldsymbol{\varepsilon}} \cdot \boldsymbol{x} + \boldsymbol{u}'(\boldsymbol{x}) + \boldsymbol{u}_0 \qquad \forall \boldsymbol{x} \in \mathfrak{B}, \tag{2}$$

Here, the first term represents the affine component of the displacement field, while the second term, $\boldsymbol{u}'$, indicates a periodic fluctuation that maintains identical values at each pair of corresponding points, $\boldsymbol{x}_+$ and $\boldsymbol{x}_-$, within the RVE boundary $\partial\mathfrak{B}$:

$$\boldsymbol{u}'(\boldsymbol{x}_+) = \boldsymbol{u}'(\boldsymbol{x}_-) \qquad \forall \boldsymbol{x}_+, \boldsymbol{x}_- \in \partial\mathfrak{B}. \tag{3}$$

Notably, the strain component associated with $\boldsymbol{u}'$ vanishes upon averaging due to periodicity, ensuring consistency between equations (1) and (2). In this context, $\boldsymbol{u}_0$ accounts for any rigid body motion.

Substituting equation (2) into equation (3), the Periodic Boundary Conditions (PBCs) can be expressed in terms of displacement $\boldsymbol{u}$, directly involving the macroscopic strain $\overline{\boldsymbol{\varepsilon}}$. These conditions apply to the unit cell boundaries $\partial\mathfrak{B}$ as follows:

$$\boldsymbol{u}(\boldsymbol{x}_+) - \boldsymbol{u}(\boldsymbol{x}_-) = \overline{\boldsymbol{\varepsilon}} \cdot (\boldsymbol{x}_+ - \boldsymbol{x}_-) \qquad \forall \boldsymbol{x}_+, \boldsymbol{x}_- \in \partial\mathfrak{B} \tag{4}$$

Thus, the macroscopic stress-strain behavior along a specified loading path can be obtained by solving local equilibrium with periodic boundary conditions while considering the relationships involved in transitioning between scales. This work focuses exclusively on in-plane macroscopic stress conditions. This means that the values of $\overline{\sigma}_{33}$, $\overline{\sigma}_{13}$, and $\overline{\sigma}_{23}$ are assumed to be zero, with only the remaining stress components being relevant.

3.2. Constitutive laws

Accurate characterization of the recycled composite's nonlinear behavior relies on constitutive laws that define the stress increments for given strain increments in each phase. At the mesoscale, two phases are considered: the PA6 matrix and the strands, treated as a unidirectional composite. The PA6 matrix is represented by

an elasto-plastic model [54], while the strands are described using an inelastic model coupled with anisotropic damage [55]. The following subsections provide a brief overview of these constitutive models. For detailed information on the numerical implementation, see [54, 55].

3.2.1. Constitutive law for the strands

As established in Section 2.1 via detailed microstructural investigation and implemented into the model (Section 2.2), strands are assumed to be 'degraded' unidirectional composites imbeded in matrix material. The constitutive law applied is based on a hybrid micromechanical phenomenological formulation [56, 57]. This model considers the anisotropic damage in unidirectional composites and incorporates the permanent inelastic strains. This inelastic response stems from the gradual emergence of damage, primarily induced by the growth of micro-cracks originating at the interfaces between the fibers and the matrix due to debonding. Figure 3 illustrates the micromechanical description of damage inside the strands. The stiffness reduction caused by the presence of these cracks is determined using the Mori–Tanaka approach. This is achieved by introducing a micro-crack density γ_c within the RVE of the strands. The reduction in stiffness is described by a fourth-order tensor $\mathbb{D}(\gamma_c)$, which progressively decreases the initial transverse isotropic stiffness tensor $\mathbb{C}_0$, of the undamaged unidirectional composite material. Consequently, the non-closure effect of these micro-cracks often results in permanent deformations. These deformations are represented by an inelastic strain tensor $\boldsymbol{\varepsilon_s}$, and the total strain $\boldsymbol{\varepsilon}$ is expressed as the sum of the elastic strain $\boldsymbol{\varepsilon_e}$ and the inelastic strain $\boldsymbol{\varepsilon_s}$.

$$\boldsymbol{\varepsilon} = \boldsymbol{\varepsilon_e} + \boldsymbol{\varepsilon_s} \tag{5}$$

This results in state laws governing the strands that are defined by the specific form of the Helmholtz free energy density, as follows:

$$\Psi(\boldsymbol{\varepsilon}, \boldsymbol{\varepsilon}_s, \gamma_c) = \frac{1}{2}(\boldsymbol{\varepsilon} - \boldsymbol{\varepsilon_s}) : \left[\mathbb{C}_0 - \mathbb{D}(\gamma_c)\right] : (\boldsymbol{\varepsilon} - \boldsymbol{\varepsilon_s}) \tag{6}$$

This framework has been initially developed to model damage in weft and warp yarns for woven composites [55]. A summary of the constitutive equations that describe the strands response is provided in Table 1. Identifying its parameters is challenging because conducting mechanical tests on isolated strands or yarns is impossible. Therefore, a reverse engineering process was developed to calibrate the model's parameters using quasi-static tests performed on woven composites. These calibrated values are adjusted for the strands in this study to account for varying

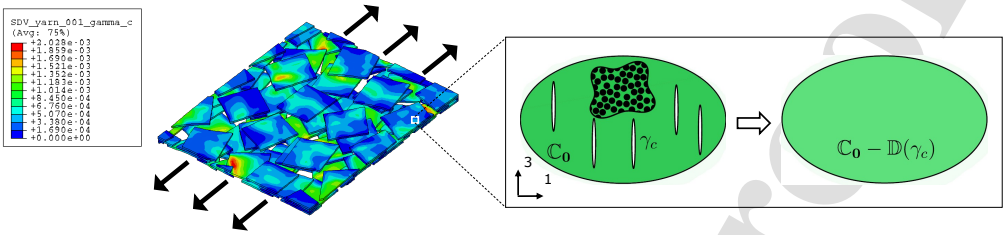

Figure 3: Micromechanical description of strand damage: UD fibers with micro-crack density γ_c influencing anisotropic damage via damage tensor $\mathbb{D}(\gamma_c)$, reducing the original stiffness tensor $\mathbb{C}_0$. (a) Illustration of strands in RVE. (b) Schematic of the strands' constitutive model.

Table 1: Summary of constitutive equations of the strands and the related variables.

Observable	Associated variable	
$\boldsymbol{\varepsilon}$	$\boldsymbol{\sigma} = \dfrac{\partial \Psi}{\partial \boldsymbol{\varepsilon}} = [\mathbb{C}_0 - \mathbb{D}(\gamma_c)] : (\boldsymbol{\varepsilon} - \boldsymbol{\varepsilon}_s)$	
Internal state	Associated variables	Evolution laws
$\boldsymbol{\varepsilon}_s$	$\boldsymbol{\sigma} = -\dfrac{\partial \Psi}{\partial \boldsymbol{\varepsilon}_s}$	$\dot{\boldsymbol{\varepsilon}}_s = \dfrac{\partial F}{\partial \boldsymbol{\sigma}} \dot{\lambda}$
γ_c	$Y_c = -\dfrac{\partial \Psi}{\partial \gamma_c}$	$\dot{\gamma}_c = \dfrac{\partial F}{\partial Y_c} \dot{\lambda} = \dot{\lambda}$ Evolution function $F(\boldsymbol{\sigma}, Y_c) = H_s(\boldsymbol{\sigma}) + Y_c$ $H_s^2 = a_{22}^2 \sigma_{22}^2 + a_{12}^2 \sigma_{12}^2$
Microscale	Local mean strain and stress in the virgin part of the material	
$\boldsymbol{\varepsilon}_0$	$\boldsymbol{\varepsilon}_0 = \mathbb{A}_0(\gamma_c) : (\boldsymbol{\varepsilon} - \boldsymbol{\varepsilon}_s)$	
$\boldsymbol{\sigma}_0$	$\boldsymbol{\sigma}_0 = \mathbb{C}_0 : \mathbb{A}_0(\gamma_c) : (\boldsymbol{\varepsilon} - \boldsymbol{\varepsilon}_s)$	
	$\mathbb{A}_0(\gamma_c)$ is the strain concentration fourth order tensor	
	Criterion	Activation ($\dot{\lambda} > 0$ if $H_c = \sup(H_c)$)
	$H_c^2 = \left[\frac{\sigma_{0_{22}}}{R_{22}}\right]^2 + \left[\frac{\sigma_{0_{12}}}{R_{12}}\right]^2$	$\gamma_c = \gamma_c^\infty \left[1 - \exp\left(-\left[\frac{\langle sup(H_c) - 1\rangle_+}{S}\right]^\beta\right)\right]$

fiber-to-matrix ratios within the strands. Additionally, the correction coefficient discussed in Section 2.2 is applied by reducing the values of Young's and shear moduli by 35% after the Mori-Tanaka micro-homogenization. The obtained values are listed in Table 2. This anisotropic damage model has been employed in multiple previous works by the authors, demonstrating its effectiveness in capturing damage evolution in composite materials. For more detailed information on its formulation and applications, readers can refer to the following citations [58, 59].

Table 2: Parameters for the constitutive model of the strands.

Feature	Parameter	value	unit
Transversely isotropic stiffness tensor	$C_{0_{1111}}$	45365	MPa
(non-null components)	$C_{0_{1122}} = C_{0_{1133}}$	6745	MPa
	$C_{0_{2222}} = C_{0_{3333}}$	22101	MPa
	$C_{0_{2233}}$	7742	MPa
	$C_{0_{1212}} = C_{0_{1313}}$	8193	MPa
	$C_{0_{2323}} = \frac{1}{2}(C_{0_{2222}} - C_{0_{2233}})$	7179	MPa
Pure transverse tension threshold	R_{22}	40	MPa
Pure in-plane shear threshold	R_{12}	20	MPa
Weibull length parameter	S	12.3	-
Weibull exponent parameter	β	2.75	-
Micro-cracks saturation	γ_c^∞	0.025	-
Transverse tension anelasticity parameter	a_{22}	3.60	-
In-plane shear anelasticity parameter	a_{12}	2.15	-

3.2.2. Constitutive law for the matrix

In this study, we adopt a conventional elasto-plastic constitutive model with isotropic hardening to simplify the matrix material modeling, following the approach outlined in previous studies [60]. It is worth noticing that, while the real material presents rate-dependent behavior, in this analysis for simplification reasons this effect is suppressed. The goal is to demonstrate the feasibility of the MuTINN technique. In future studies, the viscous response of the thermoplastic polymer will be incorporated. The behavior of the matrix material is defined through the Helmholtz free energy density, expressed as:

$$\Psi(\boldsymbol{\varepsilon}, \boldsymbol{\varepsilon}_p, p) = \frac{1}{2}(\boldsymbol{\varepsilon} - \boldsymbol{\varepsilon}_p) : \mathbb{C}_e : (\boldsymbol{\varepsilon} - \boldsymbol{\varepsilon}_p) + \int_0^p R(\xi)\, \mathrm{d}\xi, \tag{7}$$

where $\mathbb{C}_e$ represents the fourth-order stiffness tensor, typically characterized for isotropic materials using Young's modulus E and Poisson's ratio ν. The harden-

ing behavior is modeled by the function $R(\xi)$, defined as:

$$R(p) = Q_1 \left(1 - \exp(-bp)\right) + Q_2 p \tag{8}$$

where Q_1, Q_2, and b are parameters governing the hardening behavior.

The values of the elasto-plastic model's parameters are identified using experimental monotonic loading tests described in [54]. The identified parameters are summarized in Table 3.

Table 3: Material parameters for the elasto-plastic matrix model.

	Parameters	Value	Unit
Young's modulus	E	2074	MPa
Poisson's ratio (standard value)	ν	0.3	-
Yield threshold	σ_y	14	MPa
Hardening parameters	Q_1	30	MPa
	Q_2	260	MPa
	b	160	-

The total strain $\boldsymbol{\varepsilon}$ is considered as an external state variable, while the plastic strain $\boldsymbol{\varepsilon}_p$ and equivalent plastic strain p are treated as internal state variables. The equations defining these state variables are given by:

$$\boldsymbol{\sigma} = \frac{\partial \Psi}{\partial \boldsymbol{\varepsilon}} \tag{9a}$$

$$\boldsymbol{\sigma} = -\frac{\partial \Psi}{\partial \boldsymbol{\varepsilon}_p} \tag{9b}$$

$$R = \frac{\partial \Psi}{\partial p} = R(p), \tag{9c}$$

where $\boldsymbol{\sigma}$ and R denote the stress and the isotropic hardening function, respectively.

3.3. Testing methodology and experimental validation of the multiscale modeling

The model is validated against experimental monotonic tensile tests [10], using strain-controlled simulations on 10 RVEs generated from the predefined ODF [10], which spans angles from -80° to 80° (Figure 4).

The matrix follows an elasto-plastic constitutive law, while an anisotropic damage model accounts for micro-crack initiation in the strands. RVEs are loaded up to 1.2% strain along 0° and 90° orientations, matching experimental conditions.

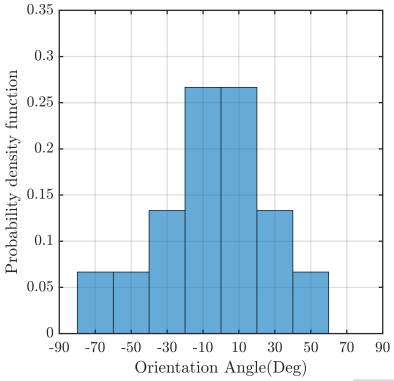

Figure 4: Adopted orientation distribution function (ODF) for the strand generation.

Figure 5 compares the numerical and experimental stress-strain curves. The mean response with a 95% confidence interval highlights variability and anisotropy. The model captures experimental trends well, with the 0° orientation results falling within the experimental range, while the 90° orientation shows a slightly stiffer response, likely due to angle discretization in the ODF.

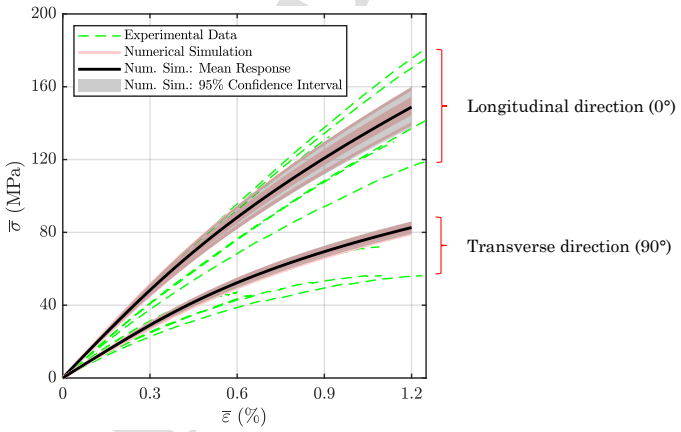

Figure 5: Numerical simulation results for 10 unit cells using the same ODF compared with experimental data. The mean response curve is shown with a 95% confidence interval (gray shaded area).

Cyclic loading-unloading tests were conducted at increasing strain levels (ε = 0.3%, 0.6%, 0.9%, and 1.2%). The strain rate during loading and unloading stages

was set to $\dot{\varepsilon} = 8 \times 10^{-3}\,\mathrm{s}^{-1}$. Unloading was performed until a near-zero load threshold ($F = 50$ N) to prevent specimen compression.

Figure 6 presents the stress-strain response for 0°, 45°, and 90° orientations, comparing experimental results (blue) with numerical simulations (red). The model accurately reproduces the material's anisotropic behavior observed in monotonic tests. Hysteresis loops are evident across all orientations, with the 90° direction showing the most pronounced loops, while the 0° direction exhibits minimal hysteresis. The intermediate 45° orientation follows a gradual transition between these two behaviors.

These results confirm the model's ability to reproduce cyclic response trends and capture the anisotropic hysteresis behavior observed experimentally.

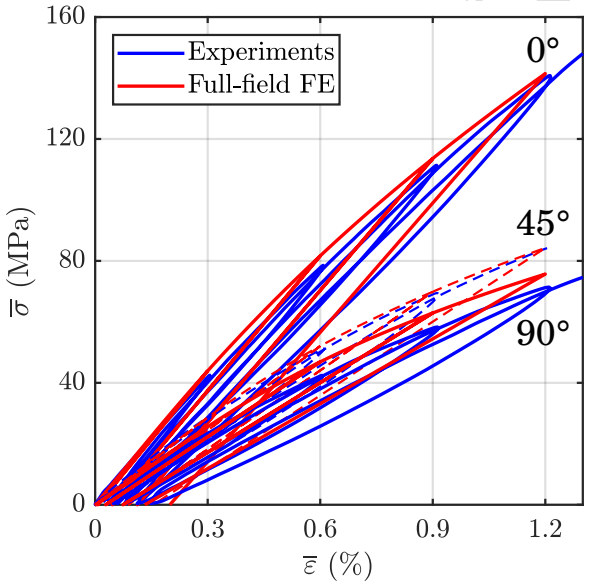

Figure 6: Comparison of experimental (blue) and numerical (red) stress-strain responses for cyclic loading-unloading tests at increasing strain levels ($\varepsilon = 0.3\%$, 0.6%, 0.9%, and 1.2%) for 0°, 45°, and 90° orientations. The 45° orientation is represented with dashed lines, highlighting its intermediate behavior between 0° and 90°.

4. MuTINN model: defining quantities of interest and model architecture

4.1. Definition and selection of quantities of interest for MuTINN model

Unlike memory-based Artificial Neural Networks like RNNs [61, 41], which rely on previous inputs to predict future behavior, the MuTINN model [49] eliminates this

dependency by introducing a phenomenological framework that accurately describes the inelastic behavior of RVEs. However, this approach requires additional variables to effectively account for the history-dependent nature of nonlinear material behavior. In homogenization theories, these variables originate at the microscale as Internal State Variables (ISV), representing specific microscopic behaviors. Including the entire ISVs can significantly increase computational demands during model training due to the larger input dimensions. A larger input size means more nodes in the neural network's input layer, leading to more connections (weights) between the input and the first hidden layer. To overcome this issue, the MuTINN model introduces specialized variables called "quantities of interest ($\overline{\boldsymbol{v}}$)," defined at the macroscopic level. Derived by averaging specific ISVs across the composite components $\mathfrak{B}_i$ (e.g., the matrix), these variables offer valuable insights by tracking metrics such as damage density and accumulated plastic strain.

For the matrix phase $\mathfrak{B}_0$, four key quantities of interest are defined: $\overline{v}_1$, $\overline{v}_2$, $\overline{v}_3$, and $\overline{v}_4$. These represent the average accumulated plastic strain (p) and the average in-plane plastic strain components ε_{p11}, ε_{p22}, and $2\varepsilon_{p12}$ within the matrix. Their mathematical expressions are as follows:

$$\forall \boldsymbol{x} \in \mathfrak{B}_0 \begin{cases} \overline{v}_1(t) = \dfrac{1}{V_0} \displaystyle\int_{\mathfrak{B}_0} p(\boldsymbol{x}, t)\ \mathrm{d}V, \\ \overline{v}_2(t) = \dfrac{1}{V_0} \displaystyle\int_{\mathfrak{B}_0} \varepsilon_{p11}(\boldsymbol{x}, t)\ \mathrm{d}V, \\ \overline{v}_3(t) = \dfrac{1}{V_0} \displaystyle\int_{\mathfrak{B}_0} \varepsilon_{p22}(\boldsymbol{x}, t)\ \mathrm{d}V, \\ \overline{v}_4(t) = \dfrac{1}{V_0} \displaystyle\int_{\mathfrak{B}_0} 2\varepsilon_{p12}(\boldsymbol{x}, t)\ \mathrm{d}V, \end{cases} \tag{10}$$

where V_0 represents the volume occupied by matrix phase.

Although the same internal state variables are defined for all strands, their evolution under loading varies based on orientation due to the anisotropic damage model. This variation complicates the selection of macroscale quantities that effectively represent the strands' behavior while minimizing information loss. To address this, four sets of quantities of interest are defined according to strand orientation. This classification is based on the original generation ODF, depicted in Figure 4, which spans angles from $-80°$ to $80°$. Given that negative angles exhibit the same mechanical behavior as their positive counterparts, they are treated as positive values for simplification. The strands are categorized into four orientation intervals: $[0°, 16°[$, $[16°, 32°[$, $[32°, 40°[$, and $[40°, 80°[$, assuming similar behavior within each interval.

This classification allows the definition of the following quantities: $\overline{v}_i$ for Strand phase 1 ($\mathfrak{B}_1$) with $i = 5, 6, 7$, $\overline{v}_j$ for Strand phase 2 ($\mathfrak{B}_2$) with $j = 8, 9, 10$, $\overline{v}_k$ for Strand phase 3 ($\mathfrak{B}_3$) with $k = 11, 12, 13$, and $\overline{v}_l$ for Strand phase 4 ($\mathfrak{B}_4$) with $l = 14, 15, 16$. Figure 7 illustrates the probability distribution of the strands over these intervals and shows the different domains ($\mathfrak{B}_1$, $\mathfrak{B}_2$, $\mathfrak{B}_3$, $\mathfrak{B}_4$) alongside the matrix phase $\mathfrak{B}_0$. The corresponding mathematical expressions for each defined quantity are provided below:

$$\forall \boldsymbol{x} \in \mathfrak{B}_1 \begin{cases} \overline{v}_5(t) = \dfrac{1}{V_1} \displaystyle\int_{\mathfrak{B}_1} \gamma_c(\boldsymbol{x}, t)\ \mathrm{d}V, \\ \overline{v}_6(t) = \dfrac{1}{V_1} \displaystyle\int_{\mathfrak{B}_1} \varepsilon_{s_{22}}(\boldsymbol{x}, t)\ \mathrm{d}V, \\ \overline{v}_7(t) = \dfrac{1}{V_1} \displaystyle\int_{\mathfrak{B}_1} 2\varepsilon_{s_{12}}(\boldsymbol{x}, t)\ \mathrm{d}V, \end{cases} \tag{11}$$

$$\forall \boldsymbol{x} \in \mathfrak{B}_2 \begin{cases} \overline{v}_8(t) = \dfrac{1}{V_2} \displaystyle\int_{\mathfrak{B}_2} \gamma_c(\boldsymbol{x}, t)\ \mathrm{d}V, \\ \overline{v}_9(t) = \dfrac{1}{V_2} \displaystyle\int_{\mathfrak{B}_2} \varepsilon_{s_{22}}(\boldsymbol{x}, t)\ \mathrm{d}V, \\ \overline{v}_{10}(t) = \dfrac{1}{V_2} \displaystyle\int_{\mathfrak{B}_2} 2\varepsilon_{s_{12}}(\boldsymbol{x}, t)\ \mathrm{d}V, \end{cases} \tag{12}$$

$$\forall \boldsymbol{x} \in \mathfrak{B}_3 \begin{cases} \overline{v}_{11}(t) = \dfrac{1}{V_3} \displaystyle\int_{\mathfrak{B}_3} \gamma_c(\boldsymbol{x}, t)\ \mathrm{d}V, \\ \overline{v}_{12}(t) = \dfrac{1}{V_3} \displaystyle\int_{\mathfrak{B}_3} \varepsilon_{s_{22}}(\boldsymbol{x}, t)\ \mathrm{d}V, \\ \overline{v}_{13}(t) = \dfrac{1}{V_3} \displaystyle\int_{\mathfrak{B}_3} 2\varepsilon_{s_{12}}(\boldsymbol{x}, t)\ \mathrm{d}V, \end{cases} \tag{13}$$

$$\forall \boldsymbol{x} \in \mathfrak{B}_4 \begin{cases} \overline{v}_{14}(t) = \dfrac{1}{V_4} \displaystyle\int_{\mathfrak{B}_4} \gamma_c(\boldsymbol{x}, t)\ \mathrm{d}V, \\ \overline{v}_{15}(t) = \dfrac{1}{V_4} \displaystyle\int_{\mathfrak{B}_4} \varepsilon_{s_{22}}(\boldsymbol{x}, t)\ \mathrm{d}V, \\ \overline{v}_{16}(t) = \dfrac{1}{V_4} \displaystyle\int_{\mathfrak{B}_4} 2\varepsilon_{s_{12}}(\boldsymbol{x}, t)\ \mathrm{d}V, \end{cases} \tag{14}$$

where V_1, V_2, V_3 and V_4 represent the volumes of the strand phases $\mathfrak{B}_1$, $\mathfrak{B}_2$, $\mathfrak{B}_3$, and $\mathfrak{B}_4$, respectively.

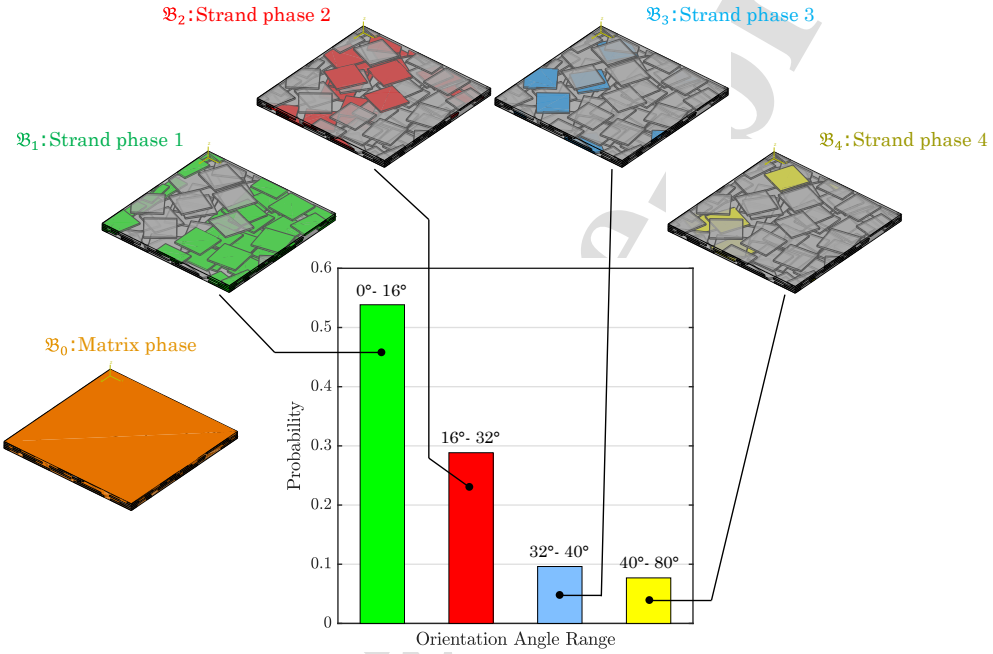

Figure 7: Probability distribution of strands over the defined orientation intervals: $[0°, 16°[$, $[16°, 32°[$, $[32°, 40°[$, and $[40°, 80°[$, showing the different domains $\mathfrak{B}_1$, $\mathfrak{B}_2$, $\mathfrak{B}_3$, and $\mathfrak{B}_4$, along with the matrix phase $\mathfrak{B}_0$.

As shown in equations 11, 12, 13, and 14, only the $\varepsilon_{s_{22}}$ and $2\varepsilon_{s_{12}}$ components of the anelastic strain tensor are considered, as these are the active components that evolve with microcrack density during in-plane loading.

4.2. Framework and structure of the MuTINN model

The Multiscale Thermodynamics-Informed Neural Network (MuTINN) is an artificial neural network (ANN) model based on thermodynamics and inspired by phenomenological constitutive models that incorporate an evolution law and a state law. Introduced in previous research [49], this model was developed for woven composites and is applied here to analyze recycled thermoplastic composite microstructures (RTPC).

MuTINN's architecture features two interconnected ANNs (Figure 8), each serving a distinct function. The first ANN defines the evolution law, processing inputs such as the current macroscopic strain components ($\overline{\boldsymbol{\varepsilon}}^n = [\overline{\varepsilon}^n_{11}, \overline{\varepsilon}^n_{22}, 2\overline{\varepsilon}^n_{12}]^{\mathrm{T}}$), the current quantities of interest ($\overline{\boldsymbol{v}}^n = [\overline{v}^n_1, \ldots, \overline{v}^n_{16}]^{\mathrm{T}}$), and the macroscopic strain increment ($\Delta\overline{\boldsymbol{\varepsilon}}^{n+1}$). It then calculates the corresponding increment ($\Delta\overline{\boldsymbol{v}}^{n+1}$).

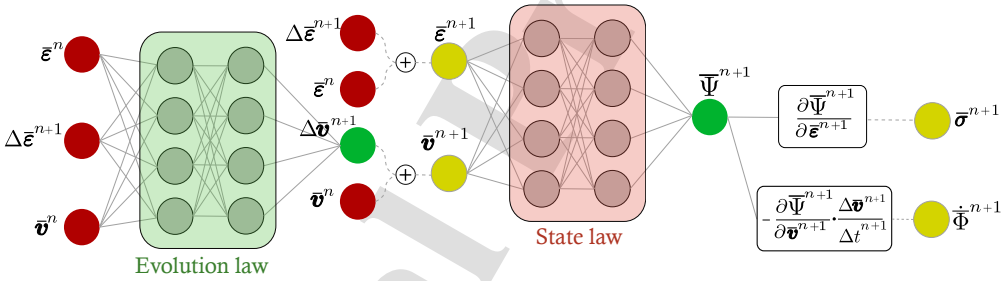

Figure 8: Architecture of the Multiscale Thermodynamics-Informed Neural Network (MuTINN), illustrating the two interconnected ANNs that define the evolution law and the state law for analyzing recycled thermoplastic composite microstructures (RTPC).

The second ANN, known as the state law model, takes the updated macroscopic strain ($\overline{\boldsymbol{\varepsilon}}^{n+1}$) and the revised quantities of interest ($\overline{\boldsymbol{v}}^{n+1}$) as inputs, predicting the Helmholtz free energy ($\overline{\Psi}^{n+1}$). Automatic differentiation is used to obtain partial derivatives of the predicted Helmholtz free energy with respect to the inputs, which is essential for calculating the macroscopic stress components ($\overline{\boldsymbol{\sigma}}^{n+1} = [\overline{\sigma}^{n+1}_{11}, \overline{\sigma}^{n+1}_{22}, \overline{\sigma}^{n+1}_{12}]^{\mathrm{T}}$) and the rate of dissipation ($\dot{\overline{\Phi}}^{n+1}$).

In the MuTINN framework, dissipation is calculated to ensure consistent thermodynamic predictions. A penalty function is incorporated to promote solutions with

positive dissipation, maintaining thermodynamic admissibility. The analysis focuses on time-independent behavior, calculating dissipation using a fixed time increment of 1 ($\Delta t = 1$).

For model training, a loss function L is defined, which is the aggregate of three distinct loss components ($L_{\overline{\boldsymbol{v}}}$, $L_{\overline{\Psi}}$, and $L_{\overline{\boldsymbol{\sigma}}}$), in addition to a penalty function, $P_{\dot{\overline{\Phi}}}$. The proposed formulation of the loss function integrates the outcomes of the two neural networks, thereby accounting for both the evolution and the state laws as considered in [45, 49, 48]. This relationship is mathematically represented by the following equation:

$$L = \lambda_{\overline{\boldsymbol{v}}} L_{\overline{\boldsymbol{v}}} + \lambda_{\overline{\Psi}} L_{\overline{\Psi}} + \lambda_{\overline{\boldsymbol{\sigma}}} L_{\overline{\boldsymbol{\sigma}}} + \lambda_{\dot{\overline{\Phi}}} P_{\dot{\overline{\Phi}}} \tag{15}$$

where $\lambda_{\overline{\boldsymbol{v}}}$, $\lambda_{\overline{\Psi}}$, $\lambda_{\overline{\boldsymbol{\sigma}}}$, and $\lambda_{\dot{\overline{\Phi}}}$ are weights assigned to each loss component: $L_{\overline{\boldsymbol{v}}}$, $L_{\overline{\Psi}}$, $L_{\overline{\boldsymbol{\sigma}}}$, and $P_{\dot{\overline{\Phi}}}$, respectively. These components represent the differences between the network's predicted outputs $\overline{\boldsymbol{v}}^{\mathrm{ANN}}$, $\overline{\Psi}^{\mathrm{ANN}}$ and $\boldsymbol{\sigma}^{\mathrm{ANN}} = \dfrac{\partial \overline{\Psi}^{\mathrm{ANN}}}{\partial \overline{\boldsymbol{\varepsilon}}}$ (representing the quantities of interest, the Helmholtz free energy and the stress, respectively) and the reference values of $\overline{\boldsymbol{v}}$, $\overline{\Psi}$, and $\overline{\boldsymbol{\sigma}}$. The equations are defined as follows:

$$\begin{cases} L_{\overline{\boldsymbol{v}}} = |\overline{\boldsymbol{v}} - \overline{\boldsymbol{v}}^{\mathrm{ANN}}|, \\ L_{\overline{\Psi}} = |\overline{\Psi} - \overline{\Psi}^{\mathrm{ANN}}|, \\ L_{\overline{\boldsymbol{\sigma}}} = |\overline{\boldsymbol{\sigma}} - \dfrac{\partial \overline{\Psi}^{\mathrm{ANN}}}{\partial \overline{\boldsymbol{\varepsilon}}}|. \end{cases} \tag{16}$$

A judicious choice of weights is crucial for ensuring accurate predictions. The MuTINN structure relies on a first neural network that predicts the increment of the quantities of interest, $\Delta \overline{\boldsymbol{v}}^{n+1}$, which is then used to predict the Helmholtz free energy. It is important to accurately predict the macroscopic quantities of interest $\overline{\boldsymbol{v}}^{n}$ by prioritizing the choice of the $\lambda_{\overline{\boldsymbol{v}}}$ weight, followed by $\lambda_{\overline{\Psi}}$, and then $\lambda_{\overline{\boldsymbol{\sigma}}}$. This accuracy is essential, as all other predictions depend on it. This makes minimizing initial inaccuracies even more critical to avoid error accumulation.

To further ensure the thermodynamic consistency of the MuTINN predictions, a penalty function $P_{\dot{\overline{\Phi}}}$ is introduced, as defined in Equation 17. This function is designed to be zero when dissipation is positive and equals the absolute value of dissipation when it is negative. By incorporating this penalty into the loss function L, the model is penalized in situations where dissipation takes on non-physical values. To this end, the weight $\lambda_{\dot{\overline{\Phi}}}$ should be greater than the other weights. This helps maintain the accuracy of predictions, especially given the potential numerical errors

introduced through automatic differentiation and the reliance on precise choices for $\lambda_{\overline{\boldsymbol{v}}}$, $\lambda_{\overline{\Psi}}$, and $\lambda_{\overline{\boldsymbol{\sigma}}}$. This penalty function is defined as follows:

$$P_{\dot{\overline{\Phi}}} = \begin{cases} 0 \quad \text{if} \quad -\dfrac{\partial \overline{\Psi}^{\mathrm{ANN}}}{\partial \overline{\boldsymbol{v}}^{\mathrm{ANN}}} \cdot \dfrac{\Delta \overline{\boldsymbol{v}}^{\mathrm{ANN}}}{\Delta t} \geq 0, \\ \left| -\dfrac{\partial \overline{\Psi}^{\mathrm{ANN}}}{\partial \overline{\boldsymbol{v}}^{\mathrm{ANN}}} \cdot \dfrac{\Delta \overline{\boldsymbol{v}}^{\mathrm{ANN}}}{\Delta t} \right| \quad \text{otherwise} \end{cases} \tag{17}$$

5. Data Generation, Results and Discussion at RVE scale

5.1. Sampling strategy and data preparation

The dataset used for training, evaluating, and testing the MuTINN model is derived from finite element computations performed in a multiscale full-field scheme on a recycled composite RVE. The unit cell is subjected to random in-plane loading paths in the longitudinal (0° manufacturing direction), transverse (90°), and in-plane shear simultaneously. The local constitutive models for the matrix and strands used in these computations are detailed in Section 3.2. These models are calibrated for tensile loading rather than compression. Therefore, simulations are stress-controlled to avoid negative stress values, ensuring valid input data for the MuTINN model and maintaining the stability of the finite element model during dataset generation. The stress intervals were chosen based on prior experimental tensile tests on the RTPC material [10], as shown in Figure 5. Stress levels are set between 0 and 200 MPa for the longitudinal direction (0°) and 0 to 150 MPa for the transverse direction (90°), with a shear stress interval of -50 to 50 MPa. It should be noted that MuTINN has been trained using one unit cell. Incorporating response variability into the MuTINN framework would require an enriched database that includes simulations for various RVEs.

The quantities of interest $\overline{v}_k$ are obtained by averaging specific ISVs defined at the microscale across the five domains $\mathfrak{B}_i$, with i ranging from 0 to 4, as described in Equations 10 to 14. The Helmholtz free energy $\overline{\Psi}$ is computed using Equation 1c, and the macroscopic strain components $\overline{\boldsymbol{\varepsilon}}^{n+1}$ are derived using Equation 1b. These quantities are then stored as input variables ($\Delta\overline{\boldsymbol{\varepsilon}}^{n+1}$, $\overline{\boldsymbol{\varepsilon}}^{n}$, $\overline{\boldsymbol{v}}^{n}$) and output variables ($\Delta\overline{\boldsymbol{v}}^{n+1}$, $\overline{\boldsymbol{\Psi}}^{n+1}$, $\overline{\boldsymbol{\sigma}}^{n+1}$) for further analysis in the MuTINN model.

In this study, we utilize a dataset of 3,300 loading paths, divided into three subsets: training (70%), validation (15%), and testing (15%). Each loading path consists of 10 discrete steps, with random stress increments applied in the longitudinal, transverse, and shear directions, as illustrated in Figure 9 where 5 examples of applied loading paths are presented. The initial steps involve lower stress levels, gradually

increasing to higher values in the final steps. This gradual progression promotes a steady evolution of damage and inelastic strain over the entire analysis, rather than a rapid change in a single step, which could hinder further evolution in subsequent steps.

To ensure sufficient data resolution, each step is further subdivided into 20 increments, yielding 200 data points per loading path and a total of 660,000 data points across the entire dataset. Among the 3,300 loading paths, 300 specifically focus on scenarios with either one active stress component while others remain zero, or two active stress components with the remaining two set to zero. These paths help to improve MuTINN's predictive accuracy for uniaxial and biaxial loading conditions.

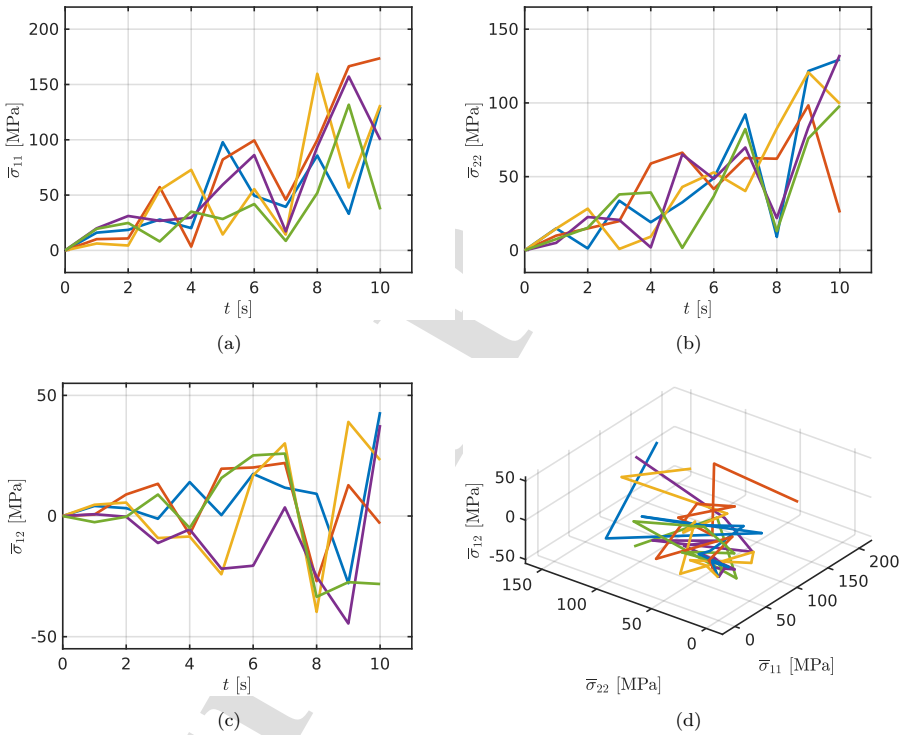

Figure 9: 3D representation of 5 out of 3300 applied loading paths, illustrating random stress increments in the longitudinal, transverse, and shear directions. The paths demonstrate a gradual increase in stress levels, promoting steady evolution of damage and inelastic strain.

5.2. Model training, validation and testing

5.2.1. Offline training process and performance evaluation

The dataset, including input and output sets, is normalized to a range of -1 to 1. The MuTINN model is then implemented using the TensorFlow framework, comprising two interconnected artificial neural networks ($\text{ANN}_{\text{evolution}}$ and $\text{ANN}_{\text{state}}$). As detailed in Table 4, each network contains two hidden layers with 64 neurons each. $\text{ANN}_{\text{evolution}}$ employs the Leaky Rectified Linear Unit (Leaky ReLU) activation function with $\alpha = 0.3$, while $\text{ANN}_{\text{state}}$ uses the Exponential Linear Unit (ELU) with $\alpha = 1$.

Table 4: Hyperparameters of the MuTINN model, detailing the structure of the ANNevolution and ANNstate networks, including hidden layers, neuron counts, and activation functions.

			MuTINN Hyperparameters		
		Inputs Layer	Hidden Layer 1	Hidden Layer 2	Output Layer
$\mathbf{ANN}_{\text{evolution}}$	Number of Neurons	22	64	64	16
	Activation function	-	leaky ReLU	leaky ReLU	Linear
$\mathbf{ANN}_{\text{state}}$	Number of Neurons	19	64	64	1
	Activation function	-	ELU	ELU	Linear

The model is trained using the Adam optimizer [62] with a batch size of 64, 1500 epochs and a learning rate of 10^{-3}, balancing the trade-off between convergence speed and stability. Mean Absolute Error (MAE) is used to evaluate the prediction accuracy of each ANN. As presented in Section 4.2, the weights $\lambda_{\overline{\boldsymbol{v}}}$, $\lambda_{\overline{\Psi}}$, $\lambda_{\overline{\boldsymbol{\sigma}}}$, and $\lambda_{\dot{\overline{\Phi}}}$ are crucial for the accuracy of the MuTINN model and are determined through multiple trials and adjustments. The optimal values identified for these weights are $\lambda_{\overline{\boldsymbol{v}}} = 5$, $\lambda_{\overline{\Psi}} = 1.5$, $\lambda_{\overline{\boldsymbol{\sigma}}} = 1.2$, and $\lambda_{\dot{\overline{\Phi}}} = 10.0$. Prioritizing the weight associated with the quantities of interest $\overline{\boldsymbol{v}}$, seems to contribute significantly to the model's performance since all other results derive from these quantities.

5.2.2. Online model assessment on unseen scenarios

Following training, the MuTINN model is first tested in the online phase by predicting mechanical responses to individual, random strain increments, assessing its performance. Figure 10 presents reference vs. prediction value curves for test data, showcasing the model's performance on unseen data. This includes one curve for the Helmholtz free energy ($\overline{\Psi}$), three for the stress components ($\overline{\boldsymbol{\sigma}}_{11}$, $\overline{\boldsymbol{\sigma}}_{22}$, and $\overline{\boldsymbol{\sigma}}_{12}$), and 16 for the quantities of interest, denoted as $\overline{\boldsymbol{v}}_i$ (with i ranging from 1 to 16). The results are satisfactory, with all values closely aligned along the diagonal line $y = x$, indicating strong predictive accuracy.

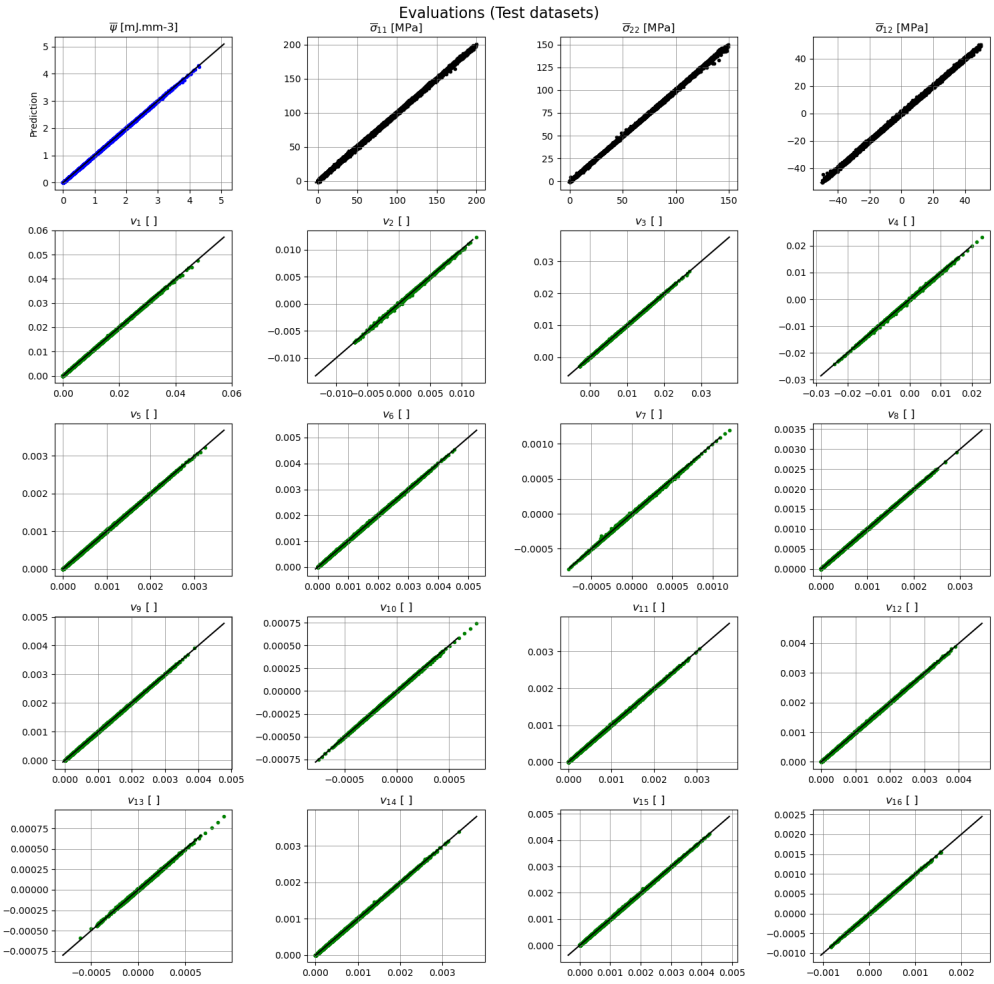

Figure 10: Reference vs. predicted values for Helmholtz free energy ($\overline{\Psi}$), stress components ($\overline{\boldsymbol{\sigma}}_{11}$, $\overline{\boldsymbol{\sigma}}_{22}$, $\overline{\boldsymbol{\sigma}}_{12}$), and the quantities of interest $\overline{\boldsymbol{v}}_i$ (with $i = 1, ..., 16$)

In the next step, the model's performance is evaluated for entire complex loading paths. The macroscopic strain increment ($\Delta\overline{\boldsymbol{\varepsilon}}^{n+1}$) serves as the input for the MuTINN, which predicts the material's response solely based on changes in the strain and the quantities of interest at each step. This approach eliminates the need for explicit knowledge of prior stress or energy states at the start of the simulation, as the model iteratively updates these quantities based on the input strain increments, as illustrated in Figure 11. The predictions for Helmholtz free energy and stress components are then compared with results from finite element (FE) periodic homogenization. Figures 12 and 13 illustrate two loading path cases, chosen to demonstrate the model's capabilities and limitations in handling complex loadings of TPRC materials.

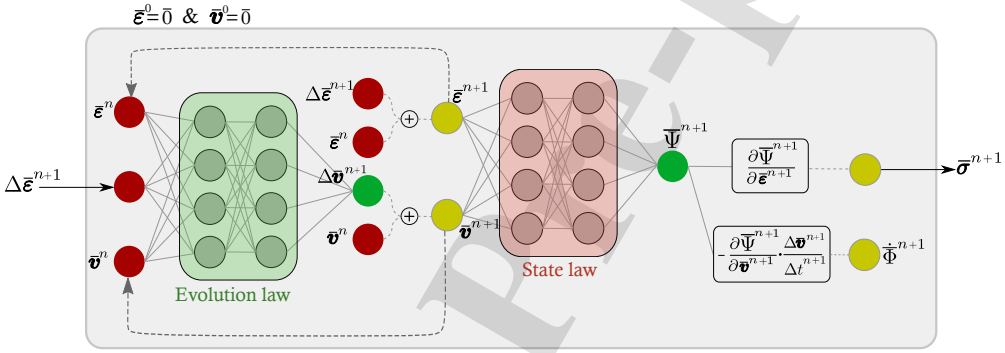

Figure 11: Architecture of the MuTINN, showing its use of macroscopic strain increments ($\Delta\overline{\boldsymbol{\varepsilon}}^{n+1}$) provided by the macroscale FE analysis to predict material responses. The model evaluates performance across complex loading paths, updating stress and energy states iteratively.

The MuTINN model accurately captures the trends of the Helmholtz free energy, as well as the $\overline{\boldsymbol{\sigma}}_{11}$, $\overline{\boldsymbol{\sigma}}_{22}$ and $\overline{\boldsymbol{\sigma}}_{12}$ stresses. Given the high variability observed experimentally (Figure 5), the MuTINN's performance is satisfactory, especially since the primary focus is on uniaxial stresses ($\overline{\boldsymbol{\sigma}}_{11}$ and $\overline{\boldsymbol{\sigma}}_{22}$).

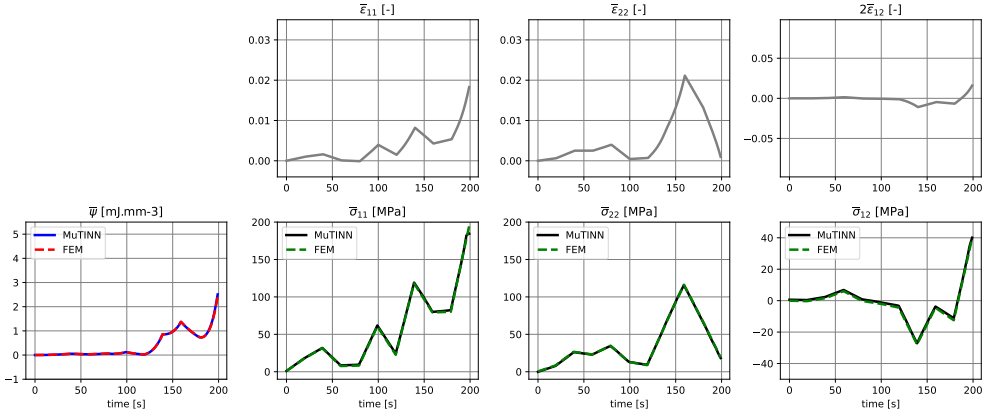

Figure 12: Comparison of MuTINN predictions and FE homogenization results for Helmholtz free energy ($\overline{\Psi}$) and stress components ($\overline{\boldsymbol{\sigma}}_{11}$, $\overline{\boldsymbol{\sigma}}_{22}$, $\overline{\boldsymbol{\sigma}}_{12}$) under unseen loading path Case 1, showing good accuracy.

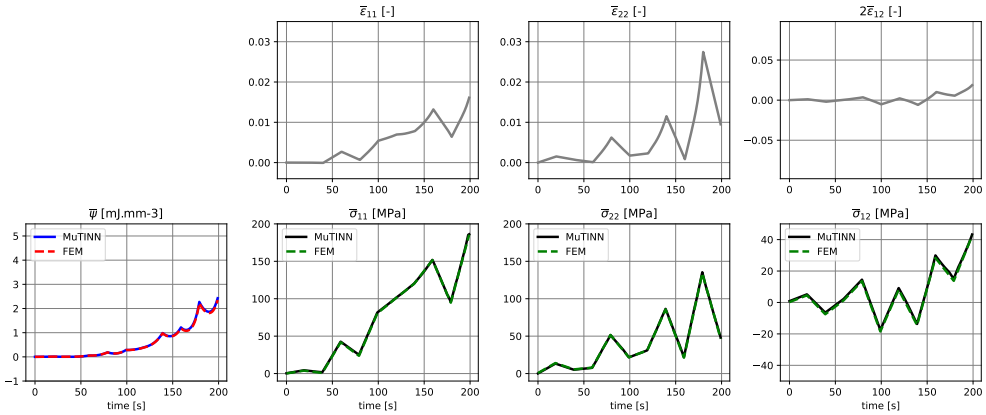

Figure 13: Comparison of MuTINN predictions and FE results for $\overline{\Psi}$, $\overline{\boldsymbol{\sigma}}_{11}$, $\overline{\boldsymbol{\sigma}}_{22}$, and $\overline{\boldsymbol{\sigma}}_{12}$ for unseen loading path Case 2.

6. Application of MuTINN for structural FE analysis for recycled composites

6.1. Overview of numerical implementation of MuTINN-FE connection

The integration of the MuTINN model into a finite element (FE) code, as described extensively in [49], is achieved through a Meta-UMAT implemented in Fortran. This Meta-UMAT serves as an interface between the FE software and the MuTINN model, enabling the calculation of macroscopic stress $\overline{\boldsymbol{\sigma}}^{n+1}$ and tangent modulus $\overline{\mathbb{C}}_t^{n+1}$ at each time increment using the given strain increment $\Delta\overline{\boldsymbol{\varepsilon}}^{n+1}$ (Figure 14). It imports the MuTINN model's parameters, including architecture, weights, and biases, from a saved file named "Properties.inp."

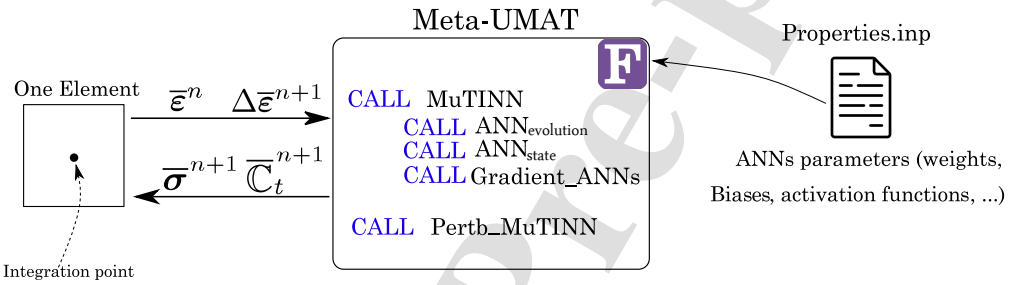

Figure 14: Schematic Implementation of MuTINN into a FE commercial software for structural computations [49].

The global FE solver also requires the macroscopic tangent operator $\overline{\mathbb{C}}_t^{n+1}$ for rapid convergence. However, an elastic operator can also be used, but it requires more iterations to achieve convergence compared to the tangent operator. To compute the latter, the "Pertb_MuTINN" function applies a perturbation technique using three elementary loading cases: $[\delta\varepsilon, 0, 0]^{\mathrm{T}}$, $[0, \delta\varepsilon, 0]^{\mathrm{T}}$, and $[0, 0, \delta\varepsilon]^{\mathrm{T}}$, with $\delta\varepsilon = 10^{-4}$.

6.2. Validation of the approach on a macroscopic point and comparison with FE computations performed on an RVE

To validate this approach, single-point computations at the macroscale (representing one element) are compared to RVE-scale calculations. Three orientations are examined: 0°, 45°, and 90°. Cyclic loading-unloading tests are performed with four cycles at increasing strain levels ($\varepsilon = 0.3\%$, $\varepsilon = 0.6\%$, $\varepsilon = 0.9\%$, $\varepsilon = 1.2\%$), unloading to zero stress. FE-MuTINN results for individual elements are compared with both experimental data and periodic homogenization at the RVE scale. Figure 15 illustrates these comparisons, with Figures 15a, 15b, and 15c showing experimental

Algorithm 1 Computation of $\overline{\mathbb{C}}_t^{n+1}$ using Pertb_MuTINN

Require: $\delta\varepsilon$, $\Delta\overline{\boldsymbol{\varepsilon}}^{n+1}$, $\overline{\boldsymbol{\varepsilon}}^{n}$, $\overline{\boldsymbol{v}}^{n}$

$\overline{\boldsymbol{\sigma}}^{n+1} \leftarrow \text{MuTINN}(\Delta\overline{\boldsymbol{\varepsilon}}^{n+1}, \overline{\boldsymbol{\varepsilon}}^{n}, \overline{\boldsymbol{v}}^{n})$

for $k = 1$ to 3 **do**

  $\Delta\overline{\boldsymbol{\varepsilon}}_{(k)}^{n+1} \leftarrow \Delta\overline{\boldsymbol{\varepsilon}}^{n+1} + \delta\bar{\varepsilon}\,[\delta_{1k}, \delta_{2k}, \delta_{3k}]^{\mathrm{T}}$, $\delta_{ij} = \begin{cases} 1 & \text{if } i = j, \\ 0 & \text{else.} \end{cases}$

  $\overline{\boldsymbol{\sigma}}_{(k)}^{n+1} \leftarrow \text{MuTINN}(\Delta\overline{\boldsymbol{\varepsilon}}_{(k)}^{n+1}, \overline{\boldsymbol{\varepsilon}}^{n}, \overline{\boldsymbol{v}}^{n})$

  $\Delta\overline{\boldsymbol{\sigma}}_{(k)}^{n+1} \leftarrow \overline{\boldsymbol{\sigma}}_{(k)}^{n+1} - \overline{\boldsymbol{\sigma}}^{n+1}$

  $\overline{\mathbb{C}}_t^{n+1}[:, k] \leftarrow \Delta\overline{\boldsymbol{\sigma}}_{(k)}^{n+1}/\delta\varepsilon$

end for

return $\overline{\mathbb{C}}_t^{n+1}$

and FE periodic homogenization results against MuTINN predictions. The results indicate strong agreement between FE and MuTINN across orientations and experimental data. However, the model slightly overestimates irreversible deformation after loading and unloading, especially for 0° and 45°, where less dissipation is observed. Deviations between the MuTINN and the experimental findings can be mainly attributed to the FEA homogenization simulations [63], which are used as source of the data-driven technique training, testing and validation. Another source of discrepancy is due to the omission of viscoelastic and viscoplastic effects in the matrix for this application. Despite this, the elastoplastic matrix model with anisotropic damage in the strand shows good accuracy compared to experimental results, and this accuracy is effectively transferred to the MuTINN model. It should be noted that the MuTINN model performs very well for the 45° unseen orientation, even though it was not explicitly trained on loading-unloading data for that orientation.

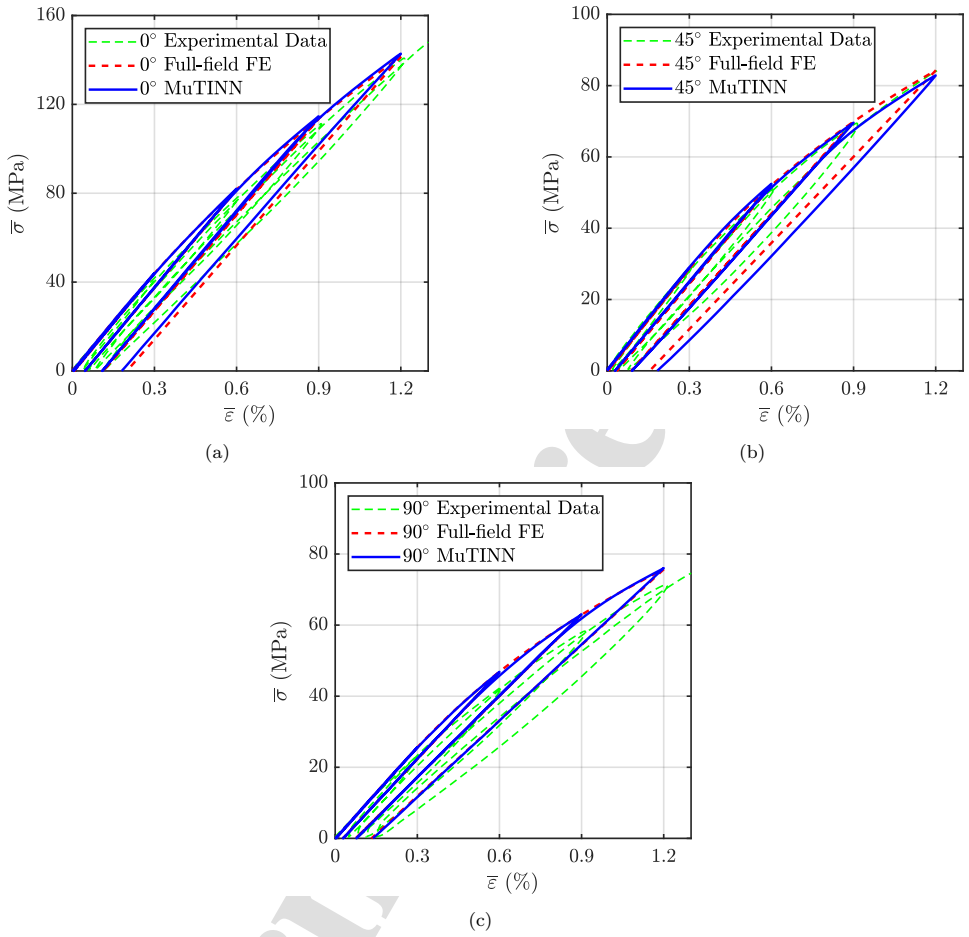

Figure 15: Comparison of numerical and experimental results for cyclic loading and unloading at increasing strain levels for various specimen orientations: (a) 0°, (b) 45° and (c) 90°. Loading and unloading stages were controlled with a strain rate of $\dot{\varepsilon} = 8 \times 10^{-3}\,\mathrm{s}^{-1}$. The MuTINN, compared to the periodic homogenization FEA, presents error in the maximum stress level of 1% at 0°, 1.6% at 45° and 0.4% at 90° orientations.

To confirm thermodynamic consistency in structural applications, MuTINN results for Helmholtz free energy ($\overline{\Psi}$), dissipation energy ($\overline{\Phi}_{\mathrm{MuTINN}}$), and strain energy ($\overline{W}_{\varepsilon}$) are compared to periodic homogenization. It is worth noting that the dissipation energy for FE - Periodic Homogenization is identified by the average dissipation of the elements N_{FE} of the total RVE. These quantities are defined as:

$$\overline{\Phi}_{\mathrm{MuTINN}} = \int_{\overline{\boldsymbol{v}}} -\frac{\partial \overline{\Psi}}{\partial \overline{\boldsymbol{v}}} \cdot \mathrm{d}\overline{\boldsymbol{v}}, \tag{18}$$

$$\overline{\Phi}_{\mathrm{FE}} = \frac{1}{V} \sum_{I=1}^{N_{\mathrm{FE}}} \Phi_I V_I, \qquad \Phi_I = \int_{ISV} -\frac{\partial \Psi_I}{\partial ISV} \cdot \mathrm{d}ISV, \tag{19}$$

$$\overline{W}_{\varepsilon} = \int_{\overline{\boldsymbol{\varepsilon}}} \overline{\boldsymbol{\sigma}} \cdot \mathrm{d}\overline{\boldsymbol{\varepsilon}} = \int_{\overline{\boldsymbol{\varepsilon}}} \frac{\partial \overline{\Psi}}{\partial \overline{\boldsymbol{\varepsilon}}} \cdot \mathrm{d}\overline{\boldsymbol{\varepsilon}}. \tag{20}$$

Φ_I represents the dissipation energy of the miscroscopic element I. Figures 16a, 16b, and 16c present energy comparisons for each configuration, highlighting the FE-MuTINN method's accuracy in predicting energy values consistent with periodic homogenization. As expected, Helmholtz free energy ($\overline{\Psi}$) and strain energy ($\overline{W}_{\varepsilon}$) are highest for the 0° orientation, indicating a stiffer response, followed by the 45° and 90° orientations. MuTINN performs well in capturing energy levels compared to classical finite element periodic homogenization. A slight discrepancy in dissipation energy ($\overline{\Phi}$) was observed at higher deformations, particularly for the 0° and 45° orientations, with the 45° orientation showing the greatest difference, as the model was not explicitly trained on this data. Additionally, the results confirm the relationship $\overline{W}_{\varepsilon} = \overline{\Psi} + \overline{\Phi}$, illustrating that strain energy is the sum of Helmholtz free energy and dissipation energy.

It is worth pointing out that applying the MuTINN approach for FE computations requires using increment values within the ranges covered during the model's training. This ensures the accuracy and reliability of the predictions, as the model is specifically trained on data within these predefined ranges. Using values outside of these ranges leads to inaccurate results especially at higher stress levels for the 0° orientation.

However, despite this limitation, the FE-MuTINN approach offers a significant advantage in terms of computational efficiency. As shown in Table 5, while traditional FE-based periodic homogenization requires several minutes per time step, FE-MuTINN completes the same computations in just a few seconds.

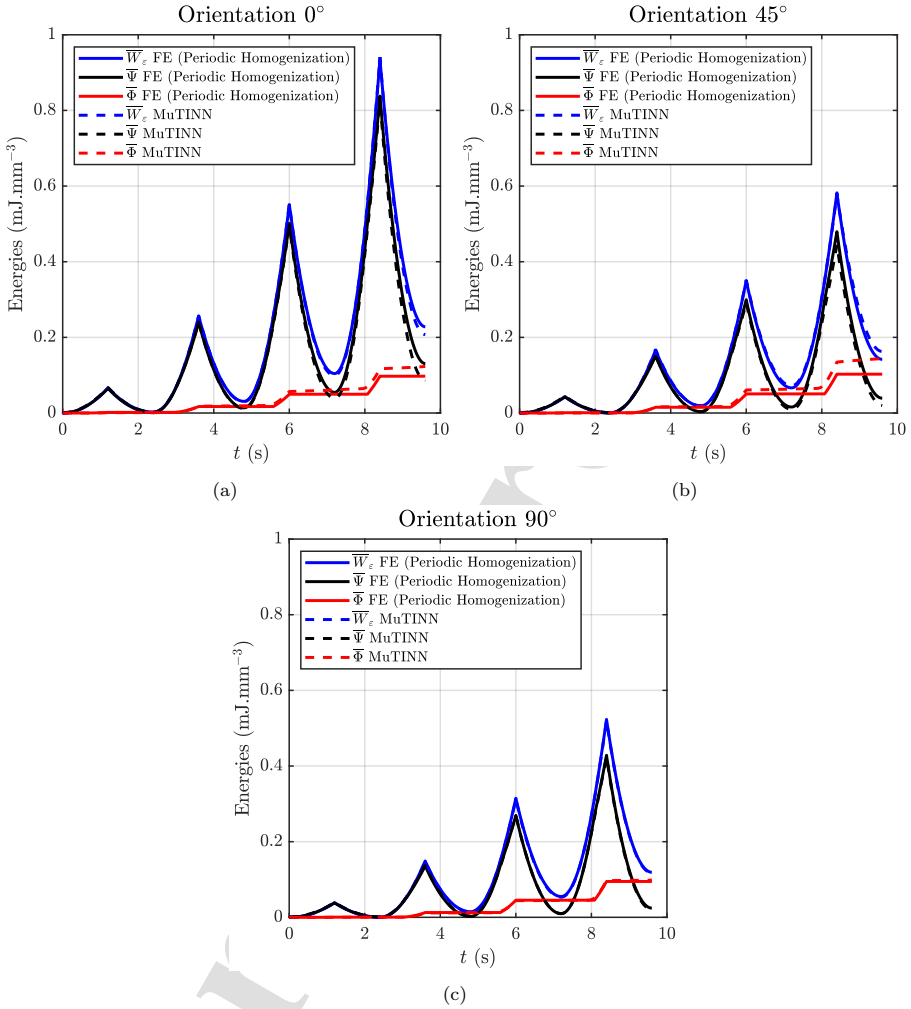

Figure 16: Energies (Helmholtz free energy, strain and dissipation energy). Comparison between FE-MuTINN and FE based periodic homogenization approach at the scale of the RVE.

Table 5: Comparison of computational time across multiple orientation for recycled composites: traditional FE-based homogenization vs. FE-MuTINN approach.

		Orientation		
	Approach	0°	45°	90°
Computation time	FE (Periodic homogenization)	1 h 08 min	1 h 20 min	1 h 07 min
	FE-MuTINN	32 s	27 s	27 s

6.3. Application case 1: structure level double notched specimen

After validating the approach on a single element and comparing the results with those from FE periodic homogenization and experimental data, a tensile test simulation at the structural level is conducted as an example. The test specimen, measuring 1000 mm in length and 300 mm in width, is analyzed with one end fixed and a 20 mm displacement applied at the other end along the y-axis (corresponding to the 90° recycled material orientation), while displacement along the x-axis remains zero. The specimen dimensions are chosen to maintain scale separation from the RVE, which measures 100 × 100 mm. Figure 17 shows the specimen geometry, boundary conditions, and approach, linking each integration point in every element to the previously described Meta-UMAT. The FE simulation has been performed in ABAQUS, using a mesh containing 616 plane stress elements of CPS3 type. The mesh size has been determined after spatial convergence analysis.

The computational time for this analysis was 47 seconds for a model containing 20 3-node plane stress elements (CPS3) and 596 4-node plane stress elements (CPS4), which is significantly faster than traditional methods like FE^2, which may take days to complete. Macroscopic strain fields are shown in Figure 18 for $\overline{\varepsilon}_{11}$ (Figure 18a), $\overline{\varepsilon}_{22}$ (Figure 18b), and $2\overline{\varepsilon}_{12}$ (Figure 18c). Expectedly, the strain levels in $\overline{\varepsilon}_{22}$—aligned with the loading direction—are the highest, especially in areas of high stress concentration.

Furthermore, Figure 19 presents macroscopic fields for selected quantities of interest, illustrating the distinct behaviors across different domains: $\overline{v}_1$ in the matrix domain $\mathfrak{B}_0$ (Figure 19a), and $\overline{v}_5$, $\overline{v}_8$, $\overline{v}_{11}$, and $\overline{v}_{14}$ in strand domains $\mathfrak{B}_1$, $\mathfrak{B}_2$, $\mathfrak{B}_3$, and $\mathfrak{B}_4$, respectively (Figures 19b–19e). The progression from $\overline{v}_5$ to $\overline{v}_{14}$ reveals increasingly distinct variations in the macroscopic fields, emphasizing the material's anisotropic nature. This trend highlights the effectiveness of the approach in which quantities of interest are distinguished based on local strand orientation, thereby capturing the anisotropic response and complex structural characteristics of the material.

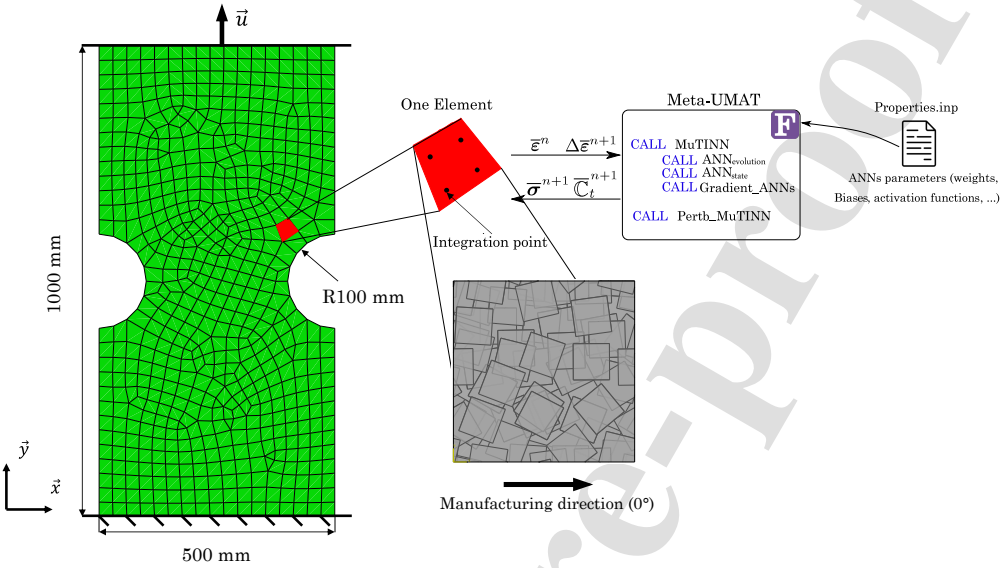

Figure 17: Geometry and boundary conditions of the tensile test specimen, illustrating the applied displacement along the y-axis with fixed x-axis displacement. Each integration point within the specimen elements is linked to the Meta-UMAT for structural analysis.

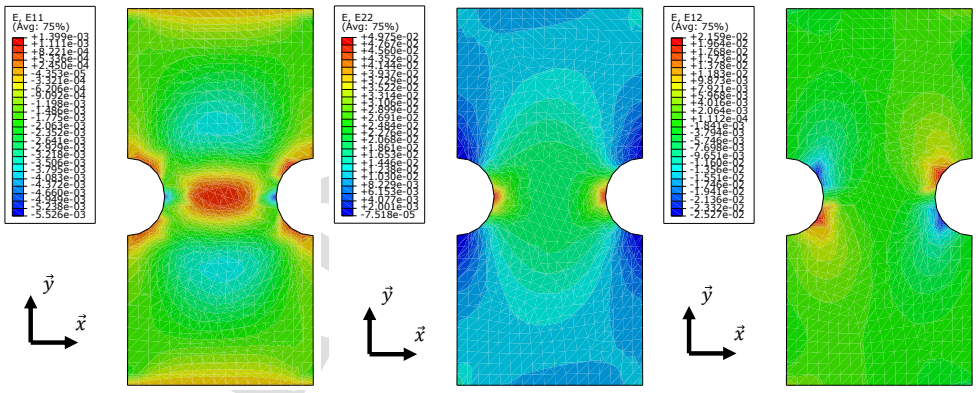

(a) $\overline{\varepsilon}_{11}$ (b) $\overline{\varepsilon}_{22}$ (c) $\overline{\varepsilon}_{12}$

Figure 18: Macroscopic strain fields from the tensile test simulation: (a) $\overline{\varepsilon}_{11}$, (b) $\overline{\varepsilon}_{22}$, and (c) $2\overline{\varepsilon}_{12}$. The results correspond to the 30th increment of the analysis for a displacement of 15 mm.

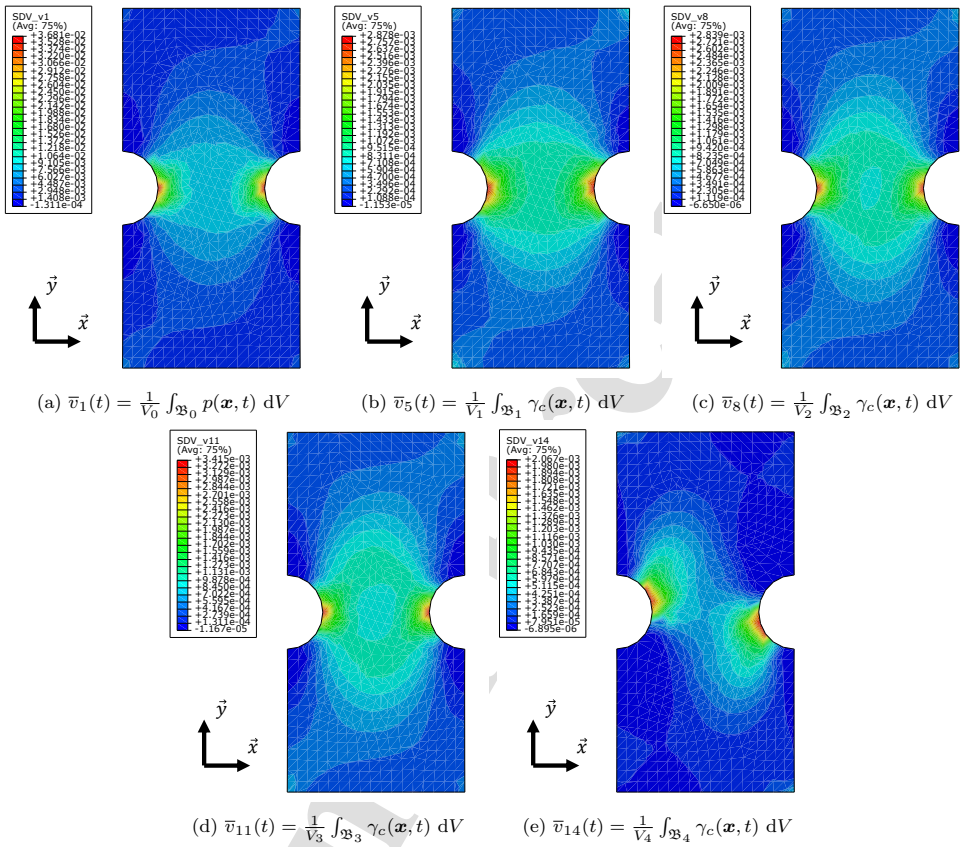

(a) $\overline{v}_1(t) = \frac{1}{V_0} \int_{\mathfrak{B}_0} p(\boldsymbol{x}, t)\, \mathrm{d}V$ (b) $\overline{v}_5(t) = \frac{1}{V_1} \int_{\mathfrak{B}_1} \gamma_c(\boldsymbol{x}, t)\, \mathrm{d}V$ (c) $\overline{v}_8(t) = \frac{1}{V_2} \int_{\mathfrak{B}_2} \gamma_c(\boldsymbol{x}, t)\, \mathrm{d}V$

(d) $\overline{v}_{11}(t) = \frac{1}{V_3} \int_{\mathfrak{B}_3} \gamma_c(\boldsymbol{x}, t)\, \mathrm{d}V$ (e) $\overline{v}_{14}(t) = \frac{1}{V_4} \int_{\mathfrak{B}_4} \gamma_c(\boldsymbol{x}, t)\, \mathrm{d}V$

Figure 19: Macroscopic fields for selected quantities of interest across different domains: (a) $\overline{v}_1$ in the matrix domain $\mathfrak{B}_0$, (b) $\overline{v}_5$ in strand domain $\mathfrak{B}_1$, (c) $\overline{v}_8$ in strand domain $\mathfrak{B}_2$, (d) $\overline{v}_{11}$ in strand domain $\mathfrak{B}_3$, and (e) $\overline{v}_{14}$ in strand domain $\mathfrak{B}_4$. The progressive variation in field characteristics from $\overline{v}_5$ to $\overline{v}_{14}$ underscores the material's anisotropy.

6.4. Application case 2: L-shaped structure

To further challenge the MuTINN model, an L-shaped structure was selected due to its complex geometry, which is expected to generate compressive stresses, particularly near the clamped region. This choice allows us to evaluate the model's performance under more demanding conditions, especially in regions where stress concentrations and compressive effects are prominent. The L-shaped structure, illustrated in Figure 20, features a hollow central section and measures 800 mm in height and 500 mm in width. The structure is clamped on one end, while a displacement of $\overline{u} = 10mm$ is applied at the other end along the y-axis. The boundary conditions and dimensions are detailed in Figure 20.

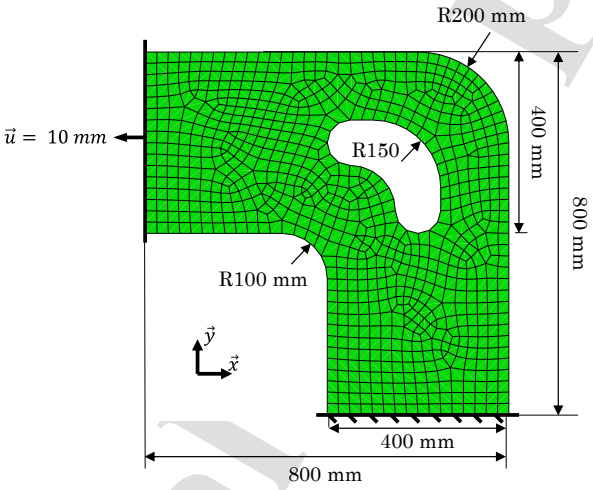

Figure 20: Geometry and boundary conditions of the L-shaped structure, showing the applied displacement along the y-axis and the clamped boundary. Each integration point within the structure elements is linked to the Meta-UMAT. Finite elements of type CPS3 and CPS4 have been used for this analysis.

The simulation results demonstrate stable convergence, with stress fields for $\overline{\sigma}_{11}$, $\overline{\sigma}_{22}$ and $\overline{\sigma}_{12}$ presented in Figures 21a–21c. As anticipated, compressive stresses are observed near the clamped region, particularly in $\overline{\sigma}_{11}$ and $\overline{\sigma}_{22}$. However, it is important to note that the model's accuracy in these regions may be limited, as it was not explicitly trained for compressive stress scenarios.

To further validate the approach, stress and strain data were computed at the centroid of a specific element within the structure, as highlighted in Figure 22. This

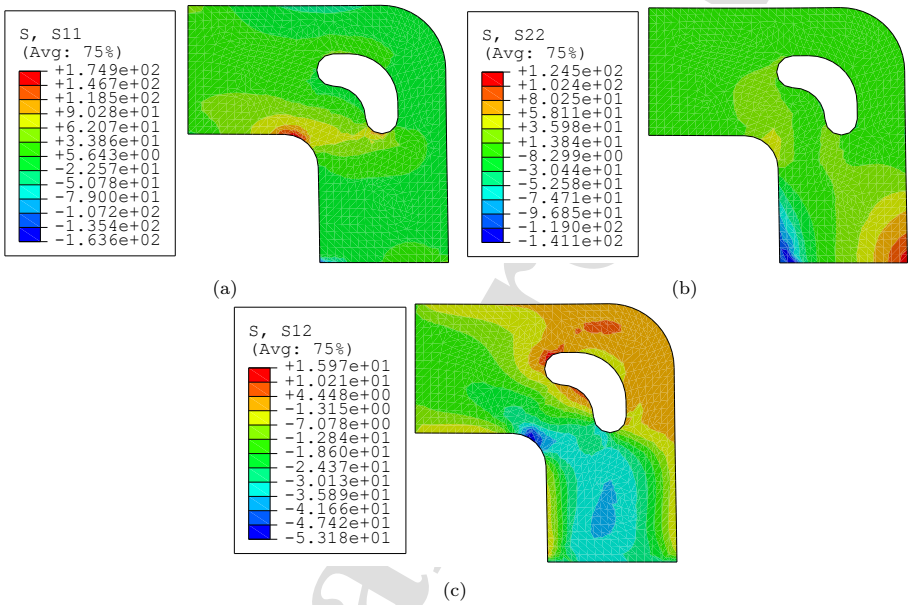

Figure 21: Macroscopic stress fields from the L-shaped structure simulation: (a) $\overline{\sigma}_{11}$, (b) $\overline{\sigma}_{22}$, and (c) $\overline{\sigma}_{12}$. Compressive stresses are observed near the clamped region, particularly in $\overline{\sigma}_{11}$ and $\overline{\sigma}_{22}$.

element was chosen due to its location in a region of moderate stress concentration, allowing for a meaningful comparison with results from periodic homogenization. The stress-strain curves for $\overline{\varepsilon}_{11}$, $\overline{\varepsilon}_{22}$ and $\overline{\varepsilon}_{12}$, computed at the centroid of the chosen element using MuTINN approach, are compared with those obtained by periodic homogenization (refence solution) in Figures 23a–23c. The good agreement between both modeling results confirms the capability of MuTINN to capture the local responses. This further supports the effectiveness of the MuTINN model in capturing the structural response of complex geometries.

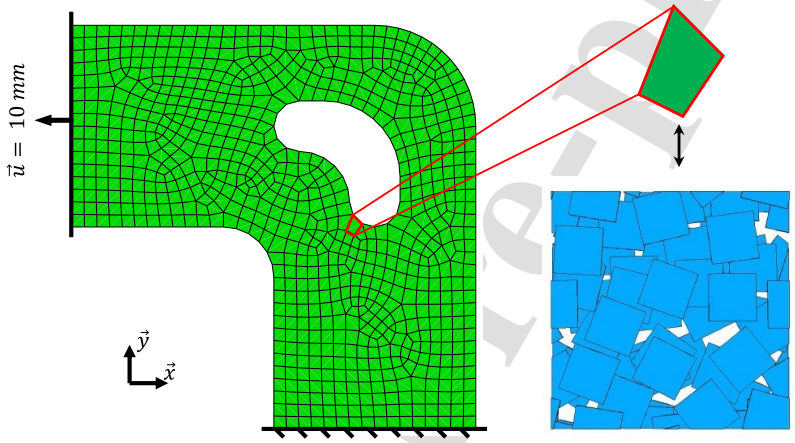

Figure 22: Highlighted element within the L-shaped structure from which stress and strain data were extracted for comparison with periodic homogenization results.

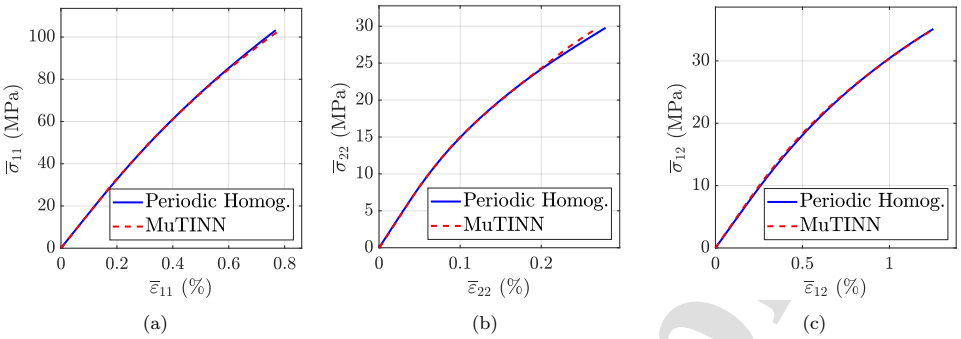

Figure 23: Comparison of stress-strain curves for the highlighted element: (a) $\overline{\sigma}_{11}-\overline{\varepsilon}_{11}$, (b) $\overline{\sigma}_{22}-\overline{\varepsilon}_{22}$, (c) $\overline{\sigma}_{12}-\overline{\varepsilon}_{12}$.

7. Conclusions and further work

This work advances the modeling of recycled thermoplastic composites through the Multiscale Thermodynamics-Informed Neural Network (MuTINN), which integrates sequential neural networks with thermodynamic principles to enable efficient macroscale simulations. Compared to traditional methods like FE^2, MuTINN significantly reduces computational time. By defining quantities of interest from microscale internal state variable averages, it eliminates the need for memory-based networks to capture loading history, accurately modeling the anisotropic and heterogeneous behavior of recycled composites. Additionally, the development of a Meta-UMAT framework ensures seamless integration into commercial finite element software, enabling efficient macroscale structural computations while maintaining a computational cost comparable to standard FEA.

MuTINN demonstrates strong predictive accuracy across various loading conditions, validated through comparisons with FE periodic homogenization and experimental data. While the model slightly overestimates irreversible deformation in some orientations due to omitted viscoelastic and viscoplastic effects, it performs robustly even for orientations not explicitly included in its training off-line data, such as the 45° orientation. Comparisons between MuTINN and periodic homogenization FEA results for experimentally studied tensile cyclic tests show error in the maximum stress level of 1% at 0°, 1.6% at 45° and 0.4% at 90° orientations. At the structural level, MuTINN has been efficiently applied for FEA analysis of complex geometries, accurately predicting macroscopic strain fields and quantities of interest, though its performance is constrained by the training data ranges.

Future work should focus on enriching the MuTINN model by incorporating data from compressive stress cases, ensuring accurate predictions for structural computations where compressive stresses are prevalent, while maintaining thermodynamic consistency. Additionally, extending the model to account for time-dependent behaviors, such as viscoelasticity and viscoplasticity, would enhance its ability to capture the full spectrum of material responses under diverse loading conditions. Another important aspect for future development is the incorporation of stochastic approach in MuTINN to capture the process induced microstructure variability and the related uncertainty on the overall response of the recycled composite [64]. While this work established a link between the microstructure of recycled composites and their mechanical performance, further research should aim to develop data-driven models that connect processing parameters to microstructural evolution. This would create a closed-loop framework, accelerating the development and optimization of recycled materials by integrating process-microstructure-performance relationships into a unified predictive tool.

Acknowledgments

This work has been conducted in the framework of the project UpCyclComp-CaMéX-IA consortium (Campus des Métiers et des Qualifications d'Excellence) de la région Grand Est funded in the framework of PIA3 (2021-2028). The authors gratefully acknowledge CETIM for supporting this work, providing the test materials along with the shared knowledge and practical procedures. They also acknowledge the support of the High Performances Computation Center (HPC - Cassiopée) of Arts et Métiers Institute of Technology, which was made available to carry out the research and the related numerical results reported in this paper.

References

[1] E. Asmatulu, J. Twomey, M. Overcash, Recycling of fiber-reinforced composites and direct structural composite recycling concept, Journal of Composite Materials 48 (2014) 593–608.

[2] M. F. Khurshid, M. Hengstermann, M. M. B. Hasan, A. Abdkader, C. Cherif, Recent developments in the processing of waste carbon fibre for thermoplastic composites–a review, Journal of Composite Materials 54 (2020) 1925–1944.

[3] P. Kiss, W. Stadlbauer, C. Burgstaller, H. Stadler, S. Fehringer, F. Haeuserer, V.-M. Archodoulaki, In-house recycling of carbon- and glass fibre-reinforced thermoplastic composite laminate waste into high-performance sheet materials, Composites Part A: Applied Science and Manufacturing 139 (2020) 106110.

[4] M. I. A. Rasheed, Compression molding of chopped woven thermoplastic composite flakes (2016).

[5] R. M. Gonçalves, A. Martinho, J. P. Oliveira, Recycling of reinforced glass fibers waste: Current status, Materials 15 (2022) 1596.

[6] G. Colucci, O. Ostrovskaya, A. Frache, B. Martorana, C. Badini, The effect of mechanical recycling on the microstructure and properties of pa66 composites reinforced with carbon fibers, Journal of Applied Polymer Science 132 (29) (2015).

[7] B. Franzen, C. Klason, J. Kubat, T. Kitano, Fibre degradation during processing of short fibre reinforced thermoplastics, Composites 20 (1) (1989) 65–76.

[8] A. D. L. Subasinghe, R. Das, D. Bhattacharyya, Fiber dispersion during compounding/injection molding of pp/kenaf composites: Flammability and mechanical properties, Materials & Design 86 (2015) 500–507.

[9] M. Nachtane, F. Meraghni, G. Chatzigeorgiou, L. Harper, F. Pelascini, Multiscale viscoplastic modeling of recycled glass fiber-reinforced thermoplastic composites: Experimental and numerical investigations, Composites Part B: Engineering 242 (2022) 110087.

[10] S. E. Sekkal, F. Meraghni, G. Chatzigeorgiou, L. Peltier, N. Durand, Experimental and multi-scale investigation of the mechanical behavior of mechanically recycled glass fiber reinforced thermoplastic composites, Composites Part B: Engineering 264 (2023) 110925.

[11] R. J. Tapper, M. L. Longana, I. Hamerton, K. D. Potter, A closed-loop recycling process for discontinuous carbon fibre polyamide 6 composites, Composites Part B: Engineering 179 (2019) 107418.

[12] D. D. Howell, S. Fukumoto, Compression molding of long chopped fiber thermoplastic composites, 2014, pp. 13–16.

[13] N. Eguemann, L. Giger, M. Roux, C. Dransfeld, F. Thiebaud, D. Perreux, Compression moulding of complex parts for the aerospace with discontinuous novel and recycled thermoplastic composite materials, 19th international conference on composite materials (2013) 1–11.

[14] L. T. Harper, C. C. Qian, R. Luchoo, N. A. Warrior, 3d geometric modelling of discontinuous fibre composites using a force-directed algorithm, Journal of Composite Materials 51 (2017) 2389–2406.

[15] H. Tang, G. Zhou, Z. Chen, L. Huang, K. Avery, Y. Li, H. Liu, H. Guo, H. Kang, D. Zeng, Fatigue behavior analysis and multi-scale modelling of chopped carbon fiber chip-reinforced composites under tension-tension loading condition, Composite Structures 215 (2019) 85–97.

[16] S. G. Kravchenko, D. E. Sommer, B. R. Denos, W. B. Avery, R. B. Pipes, Structure-property relationship for a prepreg platelet molded composite with engineered meso-morphology, Composite Structures 210 (2019) 430–445.

[17] S. G. Kravchenko, D. E. Sommer, B. R. Denos, A. J. Favaloro, C. M. Tow, W. B. Avery, R. B. Pipes, Tensile properties of a stochastic prepreg platelet molded composite, Composites Part A: Applied Science and Manufacturing 124 (2019) 105507.

[18] S. Sattar, B. B. Laredo, S. G. Kravchenko, O. G. Kravchenko, Effect of platelet length and stochastic morphology on flexural behavior of prepreg platelet molded composites, Polymer Composites 44 (4) (2023) 2122–2137.

[19] E. Glikson, A. W. Woolley, Human trust in artificial intelligence: Review of empirical research, Academy of Management Annals 14 (2) (2020) 627–660.

[20] R. D. King, S. Roberts, Artificial intelligence and machine learning in science (2018).

[21] Y. Xu, X. Liu, X. Cao, C. Huang, E. Liu, S. Qian, X. Liu, Y. Wu, F. Dong, C.-W. Qiu, et al., Artificial intelligence: A powerful paradigm for scientific research, The Innovation 2 (4) (2021).

[22] F. Chinesta, E. Cueto, Empowering engineering with data, machine learning and artificial intelligence: a short introductive review, Advanced Modeling and Simulation in Engineering Sciences 9 (1) (2022) 21.

[23] R. Ibanez, E. Abisset-Chavanne, J. V. Aguado, D. Gonzalez, E. Cueto, F. Chinesta, A manifold learning approach to data-driven computational elasticity and inelasticity, Archives of Computational Methods in Engineering 25 (2018) 47–57.

[24] J. Wei, X. Chu, X.-Y. Sun, K. Xu, H.-X. Deng, J. Chen, Z. Wei, M. Lei, Machine learning in materials science, InfoMat 1 (3) (2019) 338–358.

[25] H. L. Cheung, M. Mirkhalaf, A multi-fidelity data-driven model for highly accurate and computationally efficient modeling of short fiber composites, Composites Science and Technology 246 (2024) 110359.

[26] F. Ghavamian, A. Simone, Accelerating multiscale finite element simulations of history-dependent materials using a recurrent neural network, Computer Methods in Applied Mechanics and Engineering 357 (2019) 112594.

[27] L. Wu, N. G. Kilingar, L. Noels, et al., A recurrent neural network-accelerated multi-scale model for elasto-plastic heterogeneous materials subjected to random cyclic and non-proportional loading paths, Computer Methods in Applied Mechanics and Engineering 369 (2020) 113234.

[28] X. Liu, S. Tian, F. Tao, W. Yu, A review of artificial neural networks in the constitutive modeling of composite materials, Composites Part B: Engineering 224 (2021) 109152.

[29] J. Jiang, J. Wu, Q. Chen, G. Chatzigeorgiou, F. Meraghni, Physically informed deep homogenization neural network for unidirectional multiphase/multi-inclusion thermoconductive composites, Computer Methods in Applied Mechanics and Engineering 409 (2023) 115972.

[30] J. P. Stöcker, E. S. Elsayed, F. Aldakheel, M. Kaliske, Fe-nn: Efficient-scale transition for heterogeneous microstructures using neural networks, PAMM 23 (3) (2023) e202300011.

[31] Z. Liu, O. L. Kafka, C. Yu, W. K. Liu, Data-driven self-consistent clustering analysis of heterogeneous materials with crystal plasticity, Advances in Computational Plasticity: A Book in Honour of D. Roger J. Owen (2018) 221–242.

[32] F. Chinesta, P. Ladeveze, E. Cueto, A short review on model order reduction based on proper generalized decomposition, Archives of Computational Methods in Engineering 18 (4) (2011) 395–404.

[33] S. Metoui, E. Pruliere, A. Ammar, F. Dau, I. Iordanoff, A multiscale separated representation to compute the mechanical behavior of composites with periodic microstructure, Mathematics and Computers in Simulation 144 (2018) 162–181.

[34] M. El Fallaki Idrissi, F. Praud, V. Champaney, F. Chinesta, F. Meraghni, Multiparametric modeling of composite materials based on non-intrusive pgd informed by multiscale analyses: Application for real-time stiffness prediction of woven composites, Composite Structures 302 (2022) 116228.

[35] J. Wu, J. Jiang, Q. Chen, G. Chatzigeorgiou, F. Meraghni, Deep homogenization networks for elastic heterogeneous materials with two-and three-dimensional periodicity, International Journal of Solids and Structures (2023) 112521.

[36] Z. Liu, C. Wu, M. Koishi, A deep material network for multiscale topology learning and accelerated nonlinear modeling of heterogeneous materials, Computer Methods in Applied Mechanics and Engineering 345 (2019) 1138–1168.

[37] S. Gajek, M. Schneider, T. Böhlke, An fe–dmn method for the multiscale analysis of short fiber reinforced plastic components, Computer Methods in Applied Mechanics and Engineering 384 (2021) 113952.

[38] S. Gajek, M. Schneider, T. Böhlke, An fe-dmn method for the multiscale analysis of thermomechanical composites, Computational Mechanics 69 (5) (2022) 1087–1113.

[39] Q. Chen, R. Jia, S. Pang, Deep long short-term memory neural network for accelerated elastoplastic analysis of heterogeneous materials: An integrated data-driven surrogate approach, Composite Structures 264 (2021) 113688.

[40] E. Ghane, M. Fagerström, M. Mirkhalaf, Recurrent neural networks and transfer learning for elasto-plasticity in woven composites, arXiv preprint arXiv:2311.13434 (2023).

[41] B. El Said, Predicting the non-linear response of composite materials using deep recurrent convolutional neural networks, International Journal of Solids and Structures 276 (2023) 112334.

[42] G. E. Karniadakis, I. G. Kevrekidis, L. Lu, P. Perdikaris, S. Wang, L. Yang, Physics-informed machine learning, Nature Reviews Physics 3 (6) (2021) 422–440.

[43] E. Cueto, F. Chinesta, Thermodynamics of learning physical phenomena, Archives of Computational Methods in Engineering (2023) 1–14.

[44] M. Eghbalian, M. Pouragha, R. Wan, A physics-informed deep neural network for surrogate modeling in classical elasto-plasticity, Computers and Geotechnics 159 (2023) 105472.

[45] F. Masi, I. Stefanou, P. Vannucci, V. Maffi-Berthier, Thermodynamics-based artificial neural networks for constitutive modeling, Journal of the Mechanics and Physics of Solids 147 (2021) 104277.

[46] F. Masi, I. Stefanou, Multiscale modeling of inelastic materials with thermodynamics-based artificial neural networks (tann), Computer Methods in Applied Mechanics and Engineering 398 (2022) 115190.

[47] F. Masi, I. Stefanou, Evolution tann and the identification of internal variables and evolution equations in solid mechanics, Journal of the Mechanics and Physics of Solids 174 (2023) 105245.

[48] F. Aldakheel, E. S. Elsayed, Y. Heider, O. Weeger, Physics-based machine learning for computational fracture mechanics (2025). arXiv:2502.09025, doi:10.48550/arXiv.2502.09025.

[49] M. E. F. Idrissi, F. Praud, F. Meraghni, F. Chinesta, G. Chatzigeorgiou, Multiscale thermodynamics-informed neural networks (mutinn) towards fast and frugal inelastic computation of woven composite structures, Journal of the Mechanics and Physics of Solids 186 (2024) 105604.

[50] B. Widom, Random sequential addition of hard spheres to a volume, The Journal of Chemical Physics 44 (1966) 3888–3894.

[51] F. Praud, K. Schneider, G. Chatzigeorgiou, F. Meraghni, Microstructure generation and full-field multi-scale analyses for short fiber reinforced thermoplastics: Application to pa66gf composites, Composite Structures 341 (2024) 118175.

[52] K. Schneider, B. Klusemann, S. Bargmann, Automatic three-dimensional geometry and mesh generation of periodic representative volume elements for matrix-inclusion composites, Advances in Engineering Software 99 (2016) 177–188.

[53] K. Schneider, Computational micromechanics of matrix-inclusion composites, Ph.D. thesis (2019).

[54] F. Praud, G. Chatzigeorgiou, J. Bikard, F. Meraghni, Phenomenological multi-mechanisms constitutive modelling for thermoplastic polymers, implicit implementation and experimental validation, Mechanics of Materials 114 (2017) 9–29.

[55] F. Praud, G. Chatzigeorgiou, Y. Chemisky, F. Meraghni, Hybrid micromechanical-phenomenological modelling of anisotropic damage and anelasticity induced by micro-cracks in unidirectional composites, Composite Structures 182 (2017) 223–236.

[56] Q.-Z. Zhu, J. Shao, D. Kondo, A micromechanics-based thermodynamic formulation of isotropic damage with unilateral and friction effects, European Journal of Mechanics-A/Solids 30 (3) (2011) 316–325.

[57] M. Qi, A. Giraud, J.-B. Colliat, J.-F. Shao, A numerical damage model for initially anisotropic materials, International Journal of Solids and Structures 100 (2016) 245–256.

[58] E. Tikarrouchine, A. Benaarbia, G. Chatzigeorgiou, F. Meraghni, Non-linear fe2 multiscale simulation of damage, micro and macroscopic strains in polyamide 66-woven composite structures: Analysis and experimental validation, Composite Structures 255 (2021) 112926.

[59] F. Praud, G. Chatzigeorgiou, F. Meraghni, Fully integrated multi-scale modelling of damage and time-dependency in thermoplastic-based woven composites, International Journal of Damage Mechanics 30 (2021) 163–195.

[60] J.-L. Chaboche, A review of some plasticity and viscoplasticity constitutive theories, International journal of plasticity 24 (10) (2008) 1642–1693.

[61] A. Danoun, E. Prulière, Y. Chemisky, Thermodynamically consistent recurrent neural networks to predict non linear behaviors of dissipative materials subjected to non-proportional loading paths, Mechanics of Materials 173 (2022) 104436.

[62] D. P. Kingma, J. Ba, Adam: A method for stochastic optimization, arXiv preprint arXiv:1412.6980 (2014).

[63] S. E. Sekkal, F. Meraghni, G. Chatzigeorgiou, L. Peltier, N. Durand, Multiscale modeling of mechanically recycled glass fiber reinforced polyamide 6 composites accounting for viscoelasticity, viscoplasticity, and anisotropic damage, Composites Part B: Engineering 361 (2025) 119016. doi:10.1016/j.compstruct.2025.119016.

[64] M. J. Azzi, C. Farhat, Multimodal data-assimilation using the nonparametric probabilistic method for model-form uncertainty quantification, stochastic model updating, and digital twinning, in: AIAA SciTech Forum, American Institute of Aeronautics and Astronautics, 2024. doi:10.2514/6.2024-0578.

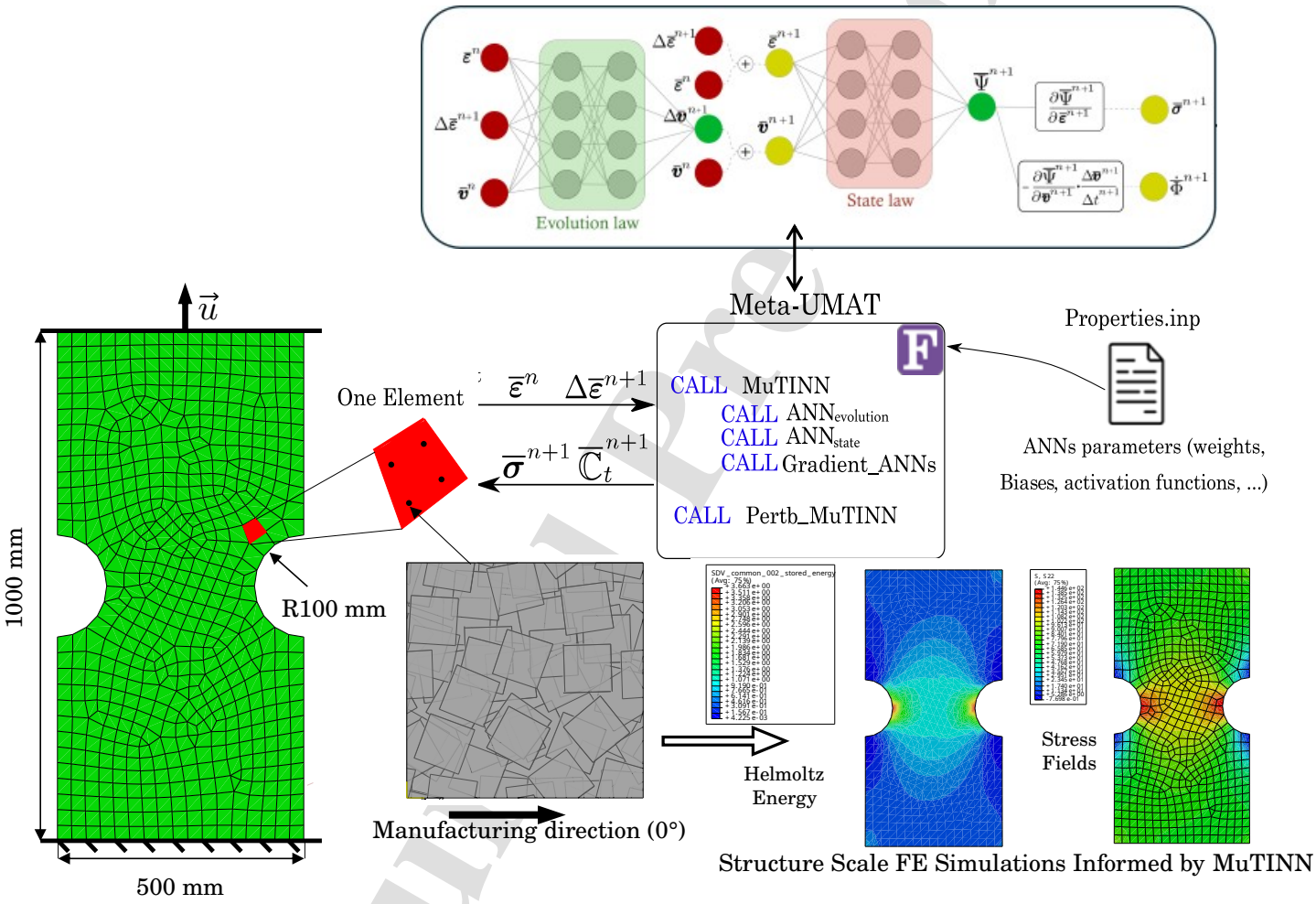

AUTHORSHIP STATEMENT Manuscript title:

Multiscale Thermodynamics-Informed Neural Networks (MuTINN) for nonlinear structural computations of recycled thermoplastic composites

Saïf Eddine Sekkal: Writing - Original Draft, Methodology, Formal Analysis, Investigation, Validation

Mohammed El Fallaki Idriss: Methodology, Investigation, Validation, Review & Editing

Fodil Meraghni: Conceptualization, Methodology, Investigation, Formal Analysis, Writing - Review & Editing, Project administration

George Chatzigeorgiou: Formal Analysis, Writing - Review & Editing, Conceptualization, Investigation

Francisco Chinesta: Conceptualization, Formal Analysis, Writing - Review & Editing.

Declaration of interests

☒ The authors declare that they have no known competing financial interests or personal relationships that could have appeared to influence the work reported in this paper.

☐The authors declare the following financial interests/personal relationships which may be considered as potential competing interests: